DESIGN AND OPTIMIZATION OF A CONFORMAL SURFACE FOR A MORPHING

SUPERSONIC AIRCRAFT

A Thesis

by

ALEJANDRO IAN MARTINEZ

Submitted to the Graduate and Professional School of
Texas A&M University
in partial fulfillment of the requirements for the degree of

MASTER OF SCIENCE

Chair of Committee,	Darren Hartl
Co-Chair of Committee,	Dimitris Lagoudas
Committee Members,	Richard Malak
Head of Department,	Ivett Leyva

August 2023

Major Subject: Aerospace Engineering

ABSTRACT

Efforts have been underway to develop a supersonic aircraft having a lower fuselage region capable of morphing. This work designs and optimizes the conformal layer in that region. Supersonic aircraft go through sub-sonic, sonic, and supersonic speeds across variable atmospheric conditions throughout a flight. Each combination of speed and atmospheric condition has a different configuration that minimizes the ground noise generated by the aircraft. The ability to morph between configurations can lessen overall ground noise as measured in Perceived Loudness in Decibels (PLdB).

The morphing component of the aircraft is composed of an adaptive five-panel system capable of reconfiguring between two primary states: a specific concave and convex shape. These panels are discrete and rigid with a conformal layer connecting and covering them. The outer surface of the conformal layer works as the outer mold line of the aircraft.

A supersonic airflow that changes direction generates pressure waves traveling at the speed of sound. These pressure waves create sonic booms when they converge, drastically increasing ground noise. Minimizing the change in airflow direction over the panel minimizes boom strength.

In this work the panel system and conformal layer are modeled using the finite element analysis software Abaqus. The final conformal layer is determined using the genetic algorithm (Non-Dominated Sorting Genetic Algorithm-II) considering two objectives. These objectives are to minimize the weighted mean magnitude of the second derivative of the outer mold line in i) the concave and ii) the convex configurations of the adaptive panel system.

The best non-dominated design was determined and used as the final design. A testing model was used to construct a prototype. Digital Image Correlation on the prototype was used to validate the Finite Element Analysis testing model. The error between the Finite Element Analysis model and the prototype was found to be small, but not negligible.

DEDICATION

To my parents, who raised me,

my grandparents, who inspired me,

and my friends who supported me.

CONTRIBUTORS AND FUNDING SOURCES

Contributors

Funding Sources

NOMENCLATURE: ACRONYMS

OGAPS	Office of Graduate & Professional Studies at Texas A&M University
B/CS	Bryan and College Station
TAMU	Texas A&M University
NASA	National Aeronautics and Space Administration
ULI	University Led Initiative
SMA	Shape Memory Alloy
PLdB	Perceived Loudness in Decibels
OML	Outer Mold Line
SL/SRL	Surface Layer/Stress-relieving Layer
CFR	Code of Federal Regulations
SIMP	Solid Isotropic Material with Penalization
TOSCA	Tool for Optimisation in Structural and Civil engineering Analyses
SPIDRS	Spatial Interpretation for the Development of Reconfigurable Structures
NSGA-II	Non-dominated sorting genetic algorithm II
AoDV	Array of Design Variables
DIC	Digital Image Correlation
CFD	Computational Fluid Dynamics
LHS	Latin Hypersquare (cube)
FF	Full Factorial
DV/OV	Design/Output Variable
CV/CC	Convex/Concave

NOMENCLATURE: SYMBOLS

Symbol	Meaning	Units
h	Specific enthalpy	$\frac{\text{J}}{\text{kg}}$
$\vec{X}$	$[X, Y, Z]$ Coordinates	m
a	Speed of sound	$\frac{\text{m}}{\text{s}^2}$
γ	Adiabatic index	—
μ, β	Mach and Shock angle	°
R	Specific gas constant	$\frac{\text{J}}{\text{kgK}}$
p	Pressure, static	$\frac{\text{N}}{\text{m}^2}$
T	Temperature	K
ρ	Density	$\frac{\text{kg}}{\text{m}^3}$
M	Mach Number	—
V	Velocity	$\frac{\text{m}}{\text{s}}$
θ	Flow Angle	—
ϕ	Twist Angle	—
c_p, c_v	Specific heat capacity at constant pressure, volume	$\frac{\text{J}}{\text{kgK}}$
e	Specific internal energy	$\frac{\text{J}}{\text{kgK}}$
r	Radius	m
J	Second polar moment of inertia	m^4
ϵ	Strain	—
σ	Stress	$\frac{\text{N}}{\text{m}^2}$
E, G	Young's Modulus, Shear Modulus	$\frac{\text{N}}{\text{m}^2}$
f	Second derivative of $Z(X)$	$\frac{1}{\text{m}}$
$\vec{n}$	Normal vector, unit	—
$\vec{D}$	AoDV	—
t	Thickness	m
O	Overhang length	m
τ	Time	s
$\vec{C}$	$= (C_{CV}, C_{CC})$ Cost function array	$\frac{1}{\text{m}}$
$\vec{F}$	Objective function	$\frac{1}{\text{m}}$
H	Side length of element	m
ζ, η	Non-dimensional coordinates	—
κ	Curvature	$\frac{1}{\text{m}}$
$\mathbf{R}, \mathbf{Z}$	Set of Real Numbers, Integers	—

TABLE OF CONTENTS

LIST OF FIGURES

xi

LIST OF TABLES

1. INTRODUCTION AND LITERATURE REVIEW

1.1 Motivation

Commercial use of supersonic aircraft has had many challenges (see Section 1.2). A significant challenge in opening up the airspace to commercial supersonic aircraft is the sonic boom created by these aircraft. Current aircraft designs are limited [1, § 91. 818] in their range of operational speeds and locations due to the sonic boom they generate (see Section 1.4). These sonic booms create varying levels of PLdB depending on the environment [2]. These varying levels greatly complicate the design of supersonic aircraft.

This thesis considers the supersonic morphing aircraft NASA ULI project (see Section 1.3). The ULI seeks to minimize the PLdB generated over a flight profile. The aircraft contains a morphing component located on the bottom side of the fuselage. The morphing component of the aircraft lowers PLdB at the ground during supersonic flight by re-configuring into a shape that minimizes the generated noise from sonic booms [3] [4]. This reconfiguration also allows for the aircraft to adjust to varying environments, although it then complicates the design of the skin.

This thesis will design and optimize the external layer of the morphing component (see Section 2.1). This work considers the worst case normal pressure scenarios along the flight profile, but not aeroelastic shear loading. Proper modelling of shear loads would require computational fluid dynamics (CFD). The morphing component uses an adaptive five-panel system and is a part of the fuselage. There are two main configurations for the panel system, convex and concave (see Section 1.6.2). In these configurations, it is not desirable for the flow to separate from the structure nor for the flow to experience drastic changes in mach number (e.g., oblique shock waves and expansion fans). Aerodynamically, structures with small changes in flow direction are less likely to cause flow separation, shock-waves (see Section 1.4.2), and expansion fans [5] [6]. This is seen and understood in many designs incorporating airfoils, including those of wind turbines [7]. Thus, this work considers minimizing the local absolute change in slope of the OML (see Section 2.1).

1

1.2 History of Commercial Supersonic Aircraft

Military use of supersonic aircraft had become commonplace by the end of the 1950s [8], but successful commercial projects proved elusive for many companies. This was mainly due to the high costs of the projects (e.g., research) and environmental factors (e.g., noise pollution). Commercial supersonic aircraft first arrived to the general public in 1976 in the form of the British Aircraft Corporation Concorde. For 27 years the Concorde transported passengers, but was impacted by numerous regulations (e.g., [1, § 91]) early on that limited the profitability of the project. These regulations limited the acceptable amount of ground noise generated by the sonic boom, especially over federal land. In August 2000 a tragic accident signalled the end of the Concorde. While the Concorde had a very safe track record overall, the small amount of aircraft could not gather enough funding for future research and maintenance. Thus, continuation of the project could not be commercially justified past 2003.

Recent interest by government agencies and corporations has resumed development of commercial supersonic aircraft technologies. This includes this work, expanded on in Section 1.3. In 2003, the NASA Shaped Sonic Boom Demonstration Program field tests showed that the intensity of the sonic boom from a Northrop F-5E (a supersonic fighter jet) can be reduced through aircraft shaping [9], particularly on the fuselage. The intensity can be reduced so much that, under normal conditions, the ground noise is below regulation limits. However, most recent developments have been computational or in controlled environments. For example, a morphing trailing edge of a wing managed to greatly reduce fuel consumption and noise for a transonic aircraft in a 2018 simulation [10]. Field testing of the Lockheed X-59, a supersonic aircraft designed for low-boom, will occur in 2023.

1.3 Overview of NASA ULI

The work contained in this thesis contributed to the supersonic morphing aircraft NASA ULI project. In 2017, NASA gave five teams the task of revolutionizing air travel. This work contributes to the Adaptive Aerostructures for Revolutionary Civil Supersonic Transportation team. This team was given the goal to figure out how the shape of an aircraft structure could change in real time to allow for relatively quiet supersonic flight with changing weather. Within the scope of this team, this thesis will mention the computational fluid dynamics work to mitigate noise generation (see Section 1.3.1) and the physical construction of the panel system (see Section 1.6.2). The computational fluid dynamics and panel design sub teams worked together to develop the demonstration panel systems in Figure 1.1b. These demonstration panel systems were prototypes for the fixed-hinge and sliding-hinge panel structures. The fixed-hinge panel system tested the effectiveness of an early conformal surface layer design while the sliding-hinge panel system adapted to simulated environmental conditions through morphing. The panel structure used in this work is further described in Section 1.6.2. Previous work from the team has shown promise in reducing ground noise with a morphing panel system creating concave and convex deformations.
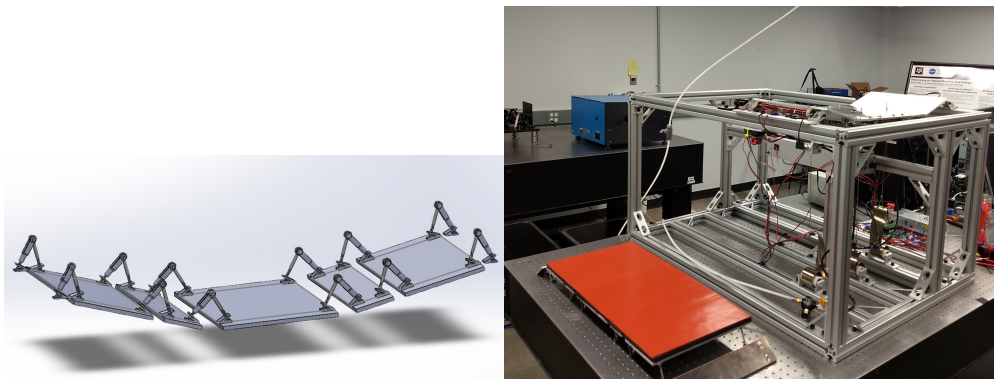
(a) Fixed-Hinge panel structure   (b) Both demonstration panel structures

Figure 1.1: The structures are similar, except for the center panel.

1.3.1   Noise Reduction

To reduce noise, first the ground pressure signature must be simulated. Initially, this was done by using the panel method based pressure distribution tool set Panel Aerodynamics (PANAIR) to generate the pressure signature near the vehicle before propagating the pressure signature to the ground using an atmospheric propagation tool, called sBOOM. The atmospheric propagation tool takes the atmospheric conditions as an input, as each environment propagates the signature differently. The ground pressure signatures were then turned into a PLdB through the use of PyLdB [11], a python code. The PLdB was used as the metric as it is universal, unlike the ground signature which could be heard differently depending on the environment. However, the panel method of PANAIR had numerous limitations and could not account for the non-linear aging of the pressure wave as it propagated from the body [12]. The pressure signature generated had significant numerical issues that cause an erroneous ground pressure signature.

Later, an equivalent area approach was developed [13]. In this approach, up to two small Gaussian distribution shaped deformations were distributed across the body of the aircraft. The perturbation in the aircraft's initial pressure signature was measured using the perturbation in the equivalent area [14]. This equivalent area approach did not solve for the best OML, but rather found locations on the aircraft where the perturbation of equivalent area led to significant decreases in PLdB.

These locations were then optimized in CFD [3]. As the areas of the aircraft that may need to change were known, the CFD analysis runs required for optimization were greatly reduced. The decrease in PLdB from the equivalent area approach was set as a target during optimization for each location. This target revealed to the CFD team how far from the likely best answer they were.

1.4 Overview of Supersonic Aerodynamic Considerations

A sound wave is a pressure wave that travels at the speed of sound (a) through a medium [15]. Across these sound waves are weak changes in the properties (and thus flow behavior) of the medium, often called a disturbance. A projectile traveling through a medium at a velocity (V) has an associated Mach number (M). A Mach number over 0.3 constantly creates sound waves that noticeably compress the flow. A wave front of these disturbances is angled μ to the initial flow direction (Equation 1.1a) before sonic flow. This wave front is called a mach wave.

To understand how flow operates through a mach wave, we follow a streamline. A streamline is the path traced out by a massless particle as it moves with the flow. As we consider laminar (attached) flow, the mass particles flow through the medium along the streamlines. The speed of sound along this streamline is determined by temperature (T), the heat capacity ratio constant (γ), and the specific gas constant (R) as seen in Equation 1.1b. The heat capacity ratio relates the heat capacity at constant pressure (c_p) to the heat capacity at constant volume (c_v). The pressure (p) and density (ρ) of the medium are related by Equation 1.1c if the medium is an ideal gas. A calorically perfect gas (Equation 1.1d) has the total enthalpy h_t across the streamline is constant (Equation 1.1e). Due to the second law of thermodynamics, the change in entropy (Equation 1.1f) must be greater than or equal to zero [6] .

$$\mu = \arcsin \frac{1}{M} \tag{1.1a}$$

$$M = \frac{V}{a} = \frac{V}{\sqrt{\gamma RT}} \tag{1.1b}$$

$$p = \rho RT \tag{1.1c}$$

$$e = c_v T \ \& \ h = c_p T = \gamma c_v T = \frac{\gamma RT}{\gamma - 1} \tag{1.1d}$$

$$h_t(X) = h(X) + \frac{V(X)^2}{2} = \text{const.} \tag{1.1e}$$

$$s(X_2) - s(X_1) = c_v \ln\left(\frac{T(X_2)}{T(X_1)}\right) - R\ln\left(\frac{p(X_2)}{p(X_1)}\right) \geq 0 \tag{1.1f}$$

1.4.1   Isentropic Flow

A mach wave is considered to be in compressible, isentropic flow. In isentropic flow, the total pressure (p_t) remains constant and no entropy is created. For isentropic flow, the local relation between mach number, static pressure, and total pressure can be found by using Equations 1.2.

$$c_v \ln\left(\frac{T_t}{T(X)}\right) = R\ln\left(\frac{p_t}{p(X)}\right) + (s(X) - s(X)) = R\ln\left(\frac{p_t}{p(X)}\right) \tag{1.2a}$$

Applying Equations 1.1d and 1.1e to Equation 1.2a:

$$\frac{p_t}{p(X)} = \frac{T_t}{T(X)}^{\gamma/(\gamma-1)} = \left(1 + \frac{V(X)^2}{2c_p T(X)}\right)^{\gamma/(\gamma-1)} \tag{1.2b}$$

Applying Equation 1.1b to Equation 1.2b:

$$\frac{p_t}{p} = \left(1 + \frac{\gamma - 1}{2}M^2\right)^{\gamma/(\gamma-1)} \tag{1.2c}$$

Only one more function is required to describe an isentropic flow regime. This function relates the flow behind and in front of the mach wave based on the overall change in flow angle between them. This function is called the Prandtl-Meyer function, $\nu(M)$ [6].

$$\nu(M) \equiv \left(\sqrt{\frac{\gamma + 1}{\gamma - 1}}\tan^{-1}\sqrt{\frac{(\gamma - 1)(M^2 - 1)}{\gamma + 1}} - \tan^{-1}\sqrt{M^2 - 1}\right) \tag{1.3a}$$

$$\Delta\theta = \begin{cases} \nu(M_2) - \nu(M_1), & \text{if declining/expanding} \\ \nu(M_1) - \nu(M_2), & \text{if inclining/compressing} \end{cases} \tag{1.3b}$$

The Equation sets 1.2 and 1.3 together show that the higher the change in flow angle ($\Delta\theta$), the larger the change in M, which induces a larger change in pressure across a mach wave, which is thus heard as a louder sound wave. If inclination is done suddenly, a shock wave is generated instead.

1.4.2   Shock Waves

Mach waves can be intensified through constructive interference to evolve into a shock wave. This is far more common during sudden changes in surface inclination, θ, but may also occur due to coalescence of mach waves after declination [16]. An example of shock generation from sudden inclination is shown in figure 1.2a. These shock waves create a stronger front that makes an angle β with the flow direction before the shock. This stronger front has a much greater change in pressure. The mach angle is considered an infinitely weak oblique shock wave from an infinitely thin airplane, as seen in Figure 1.2b [6]. The large shock generated by the thicker airplane creates a large and sudden change in pressure that is heard as a sonic boom.
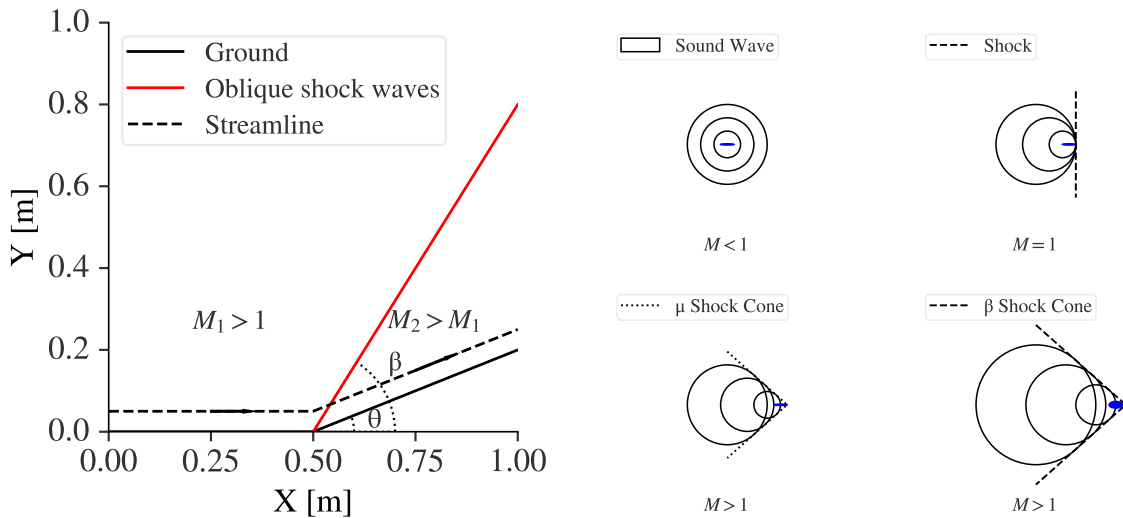
(a) Shock generation by a sudden corner.   (b) Shock generation from an aircraft.

Figure 1.2: Shock generation examples.

This strong front makes the flow non-isentropic, thus a shock wave causes a change in total pressure (unlike isentropic flow). Total enthalpy, velocity tangential to the shock, and total temperature remain the same across the wave [6]. The total enthalpy equation can be simplified to only include the component of the mach numbers normal to the shock wave. With these values retained across the shock, the ideal gas law, the simplified total enthalpy equation, and the definition of the speed of sound, a relation between the normal mach number before the shock ($M_{n,1}$) and after the shock ($M_{n,2}$) can be computed (Equation 1.4) [6].

$$M_{n,2}^2 = \frac{1 + [(\gamma - 1)/2]M_{n,1}^2}{\gamma M_{n,1}^2 - (\gamma - 1)/2} \tag{1.4}$$

The supersonic morphing aircraft is experiencing $M > 1$. This means that, along the outer mold line, the initial flow is assumed $M > 1$. To understand the implications of this, we take a simple case, shown in Figure 1.2a, with a calorically perfect gas and a velocity normal to the oblique shock wave noted by V_1. The oblique shock takes an angle β relative to the initial flow direction due to an inclination θ. The relation between the inclination angle, oblique shock angle, and the Mach number before the shock is shown in Equation 1.5c [6, pg. 624].

$$M_{n,1} = \sin(\beta)M_1 \tag{1.5a}$$

$$M_{n,2} = \sin(\beta - \theta)M_2 \tag{1.5b}$$

$$\tan(\theta) = 2\cot(\beta)\frac{M_1^2\sin^2(\beta) - 1}{M_1^2(\gamma + \cos(2\beta)) + 2} \tag{1.5c}$$

Every inclination has two possible values of shock wave angle, but the lesser angle is assumed for this application. An increasing inclination will require larger shock angles, which will create stronger pressure (or sound) waves. If the inclination is smooth, the flow remains isentropic and the pressure increases less than if it was a sharp turn. Thus, this work will seek to minimize the local mean inclination in flow direction (see 2.1).

1.5 Overview of Active Materials

When a material is meant to provide additional functionality beyond passively accommodating the loads applied to it, it is considered a multi-functional material. Materials that experience mechanical responses to non-mechanical stimuli one or two orders of magnitude higher than those resulting from conventional material behavior (e.g. , thermal expansion) are considered active materials [17, pg. 1]. The strain response to thermal stimulus is not considered purely elastic (el) nor is it considered plastic (pl). Instead, they are designated thermo-elastic (th) and in-elastic (ie). The thermal expansion and elastic strain are incorporated into the thermo-elastic strain response [17, eq. 3.3.39]. The total shear strain is the sum of all three. Thermal expansion is a volumetric non-shear strain, thus $\epsilon_{12}^{(th)} = \epsilon_{12}^{(el)}$. If we assume shear stress is only about the 1 axis along the 2 axis and the shear modulus for the material (G) is constant, then, the stress and strain equation becomes:

$$\epsilon_{12}^{(tot)} = \epsilon_{12}^{(el)} + \epsilon_{12}^{(ie)} + \epsilon_{12}^{(pl)} \tag{1.6a}$$

$$\sigma_{12} = 2G(\epsilon_{12}^{(tot)} - \epsilon_{12}^{(ie)} - \epsilon_{12}^{(pl)}) \tag{1.6b}$$

The shear stress creates a moment (m) and twist angle ($\phi(X)$) on the outer radius (r) [18]:

$$m = \frac{J\sigma_{12}}{r}, \phi(X) = \frac{2\epsilon_{12}^{(el)}X}{r} \tag{1.6c}$$

These active materials have many sources of strain. For example, applying an electric potential difference to a piezoelectric active material induces a mechanical response. The reverse is also true, as a mechanical load would induce a voltage. This coupling between the electric and mechanical properties is not exclusive, as electro-thermo-mechanical coupling can occur in materials as well [19]. However, most active materials have low specific actuation energy [17, Figure 1. 2]. An exception to this is SMA. SMAs are thermo-mechanically coupled materials exhibiting one order of magnitude more specific actuation work energy density than their nearest competitors, piezoelectric polymers. Their inelastic strain is considered to be purely from transformation (tr).

1.5.1   Shape Memory Alloy

A typical shape memory alloy (SMA) has two solid phases of different crystal structures. These phases, called austenite and martensite, have two different crystal structures. The phase change can be seen in Figure 1.3, a stress-temperature graph. Both phases can have different stiffnesses, some comparable to steel [20] and others to aluminum. Austenite begins to transform into martensite at the martensite start temperature ($T = M_s(\sigma)$ [K]) and ends transforming at the martensite finish temperature ($T = M_{f(\sigma)}$ [K]). Strain recovery can be performed through transformation from martensite to austenite, meaning that a straight wire bent then unloaded in martensite phase will become straight again in austenite phase. Some materials can also be trained through thermal cycling to do the same from austenite to martensite [17]. However, this two-way shape memory effect can be perturbed if the material experiences overloading thermally or mechanically. The inelastic strain created by a SMA is caused by the different crystal structure of each phase, rather than a chemical reaction. This martensitic transformation makes SMA very predictable, though research on fatigue is necessary for numerous cycles [21].

$$\epsilon_{12}^{(tot)} = \epsilon_{12}^{(th)} + \epsilon_{12}^{(tr)} + \epsilon_{12}^{(pl)} \tag{1.7}$$
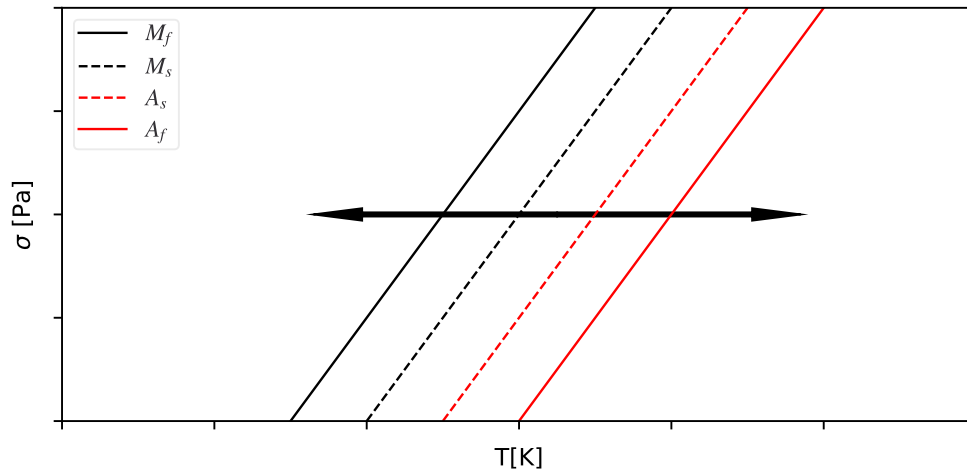
Figure 1.3: SMA Stress vs Temperature schematic

10

1.6 Adaptive Structures

1.6.1 Overview of Adaptive Structures

When a structure is meant to accommodate multiple load states without failure, it is then a multi-state structure. A multi-state structure designed for adaptation to different load states is an adaptive structure. Adaptive structures have been studied extensively in all fields, particularly in civil engineering and aerospace engineering. Civil engineers and architects created "kinetic architecture" that can move without losing structural integrity since the middle ages (e.g. , a drawbridge), but serious study on the matter started in the 1970s [22]. This study coincided with the development of many active materials (see Section 1.5). These active materials allowed for compact adaptive components that could be integrated with classical non-adaptive design approaches (e.g. , SMA torque tube and linear actuator).

Adaptive structures are well suited to multi-objective problems. This is because these adaptive structures greatly assist in multi-objective optimization by effectively optimizing a different structural state for every load state (see Section 2.1.1). A classical approach to these multi-state structures have one design passively accommodate each state. The adaptive component in a multi-state structure using the classical approach is a part of the load bearing structure directly. Meanwhile, an active approach will have the load bearing design be reconfigured by another component (e.g. , an actuator) to handle each load state. This approach allows for the non-load bearing adaptive components to be designed simultaneously with but separately from the main body. As shown in [23], an actively transforming structure outperformed a passive structure in a multi-state structure.

The NASA ULI project's supersonic aircraft will go through sub-sonic, sonic, and supersonic speeds at various atmospheric conditions throughout the flight profile [2]. The different combinations of atmospheric condition and speed create different Mach numbers (see Equation 1.1b). Thus, for this multi-state structure, an adaptive design is considered.

1.6.2 Adaptive Panel System

The adaptive structure below the conformal surface layer is composed of seven panels connected in series along the X-axis by offset hinges. The pins are along the Y-axis. As in the fixed-hinged design, the main five panels seen in Figure 1.1a are attached to the rest of the aircraft structure by two attachment panels. These panels do not move, but their hinges to the main five panels are where the torque tubes will actuate the first and fifth panel along the X axis. Of the five panels, only three were unique as seen in Figure 1.5. Panels four and five were the same size as two and one, respectively. All are 30.48 [cm] wide along the Z-axis. The fixed-hinge kinematic model from the panel development team was given rotation actuation angles and returned the reference point ($\vec{X}_i^{(Top,middle)}$) and top face normal ($\vec{n}_i^{(Top)}$) for each panel i, as represented in Figure 1.4. This panel system was not the final design due to complicating the kinematic solutions.
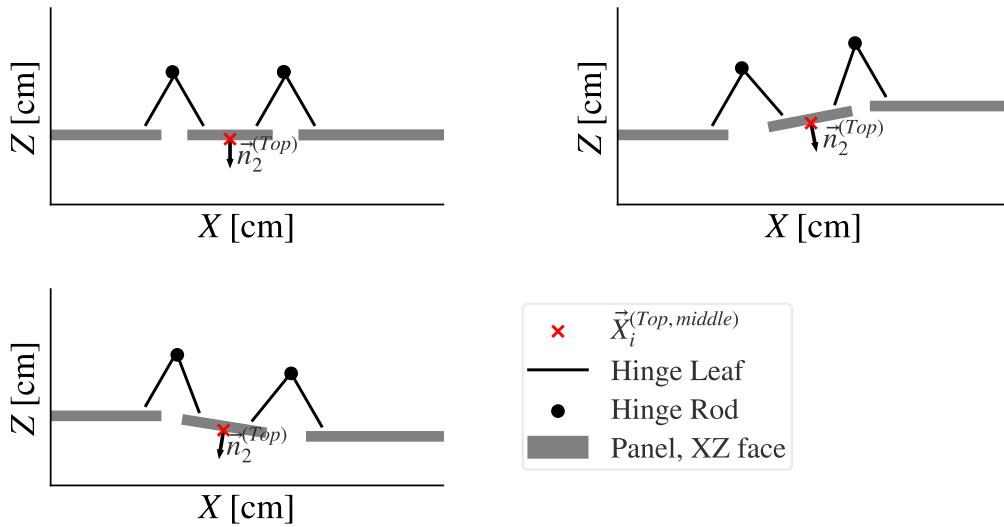
Figure 1.4: Fixed-hinge panel system in three configurations

Figure 1.5: Sizing of the unique three panels in the flat configuration

The sliding-hinge design incorporates a linear actuator (driven by a torque tube) attached to the middle of the center panel. Now with three directly actuated panels, the five panel system is better suited for symmetric transitions from one configuration to another.

For this work, an amalgam between these two designs is used. The five panel system has three configurations: flat, concave, and convex. These are described in Table 1.1. The five panel system is assumed to be symmetric across the middle of the third panel in all configurations. Thus, only three panels will be considered from henceforth. The convex and concave configurations are assumed to be equally likely in this thesis. The hinges used for the panel system are all the same and are sized according to Table 1.2. For the Abaqus model, going from one configuration to another is considered to take 5 [min]. The size measurements for the panels can be seen in Figure 1.5. The hinges are still offset from the panels.

Table 1.1: Panel Configurations

Configuration	Panel i	$\vec{X}_i^{(top,middle)}$ [cm]	$\vec{n}_i^{(top)}$
Flat	1	$(6.69, 0, 0)$	$(0, 0, -1)$
Flat	2	$(18.70, 0, 0)$	$(0, 0, -1)$
Flat	3	$(33.44, 0, 0)$	$(0, 0, -1)$
Convex	1	$(6.69, 0, 0)$	$(0, 0, -1)$
Convex	2	$(18.21, 0, -0.78)$	$(-0.158, 0, -0.988)$
Convex	3	$(32.55, 0, -1.57)$	$(0, 0, -1)$
Concave	1	$(6.69, 0, 0)$	$(0, 0, -1)$
Concave	2	$(19.78, 0, 1.22)$	$(0.189, 0, -0.982)$
Concave	3	$(35.49, 0, 2.21)$	$(0, 0, -1)$
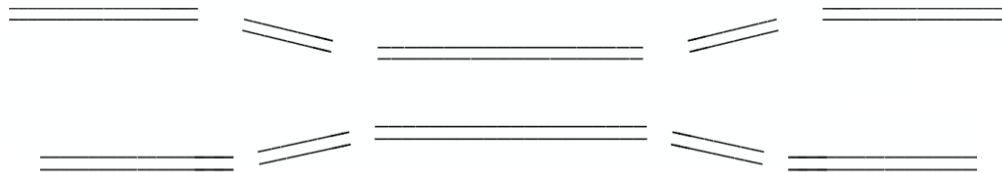
Figure 1.6: Simple diagram of the five panel system in the concave and convex configurations

Table 1.2: Hinge measurements

Side	Base face offset corner [cm]	Base angle from panel [°]	Hinge Leaf length [cm]
Left	(1. 1,0,1. 1)	60	4. 6
Right	(1. 1,0,1. 1)	60	4. 6

Figure 1.7: The hinge pin (c.f. 1.4) is connected to the base with a rod-shaped hinge leaf.

The panels are made of aluminum 2024-T4. This material is significantly stiffer [24] and denser, but with a much lower maximum elastic strain than the materials used for the conformal surface layer. This material was chosen for the prototype due to the ease of modifying the panels with the available drill bits, the light weight, and the low replacement cost.

The five panel system utilizes a SMA torque tube as an actuator (see 1.5.1 and Figure 1.8). Each torque tube is inductively heated. While many smart materials and structures could fill this actuation role, SMA torque tubes have higher work density than most active materials while allowing precise, controllable, and continuous actuation [4]. However, this torque tube does have a low actuation frequency [17, Figure 1. 2]. This frequency is not as important in the current application, which considers actuation on the time scale of atmospheric profile changes during flight. Previous work on morphing wings [25] and other components incorporate SMAs for this reason.
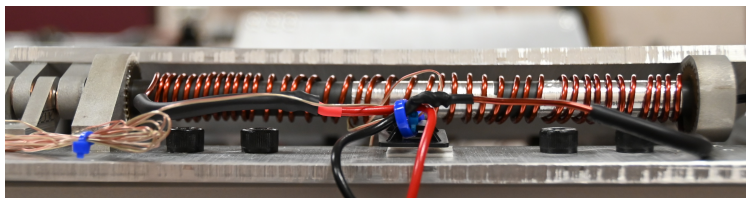
Figure 1.8: SMA torque tube with induction heating coils.

2. PROBLEM STATEMENT

2.1 The Conformal Layer

The purpose of the conformal layer is to produce and then preserve a smooth contour in multiple panel system configurations. The system is dynamic due to the movement between the different configurations on the surface. The system must consider large strains from tension and compression, as well as strain-rate dependent behavior. While the conformal layer has a pressure load of ± 0.5[psi] (see Figure 2.1) and is flexed by the panel system (see Section 1.6.2) to a strain of at least 50% in this thesis, future work could have the pressure load vary. Materials that can handle that handle large strains frequently are considered rubber-like [26]. Most rubber-like materials are modelled using the non-linear hyper-elastic models and are considered generally incompressible [27, p. 46]. Incompressible materials that are being compressed in plane must expand out of plane or buckle, creating unwanted bumps (see figure 2.1b). To counter these issues, there will be two layers, the pre-strained compliant Surface Layer and a supportive Stress-relieving Layer.
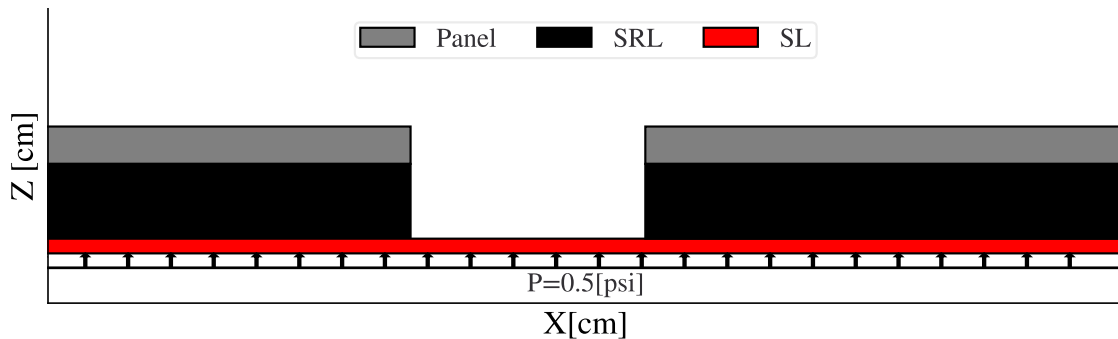
Figure 2.1: The conformal surface layer with full loading in the flat configuration
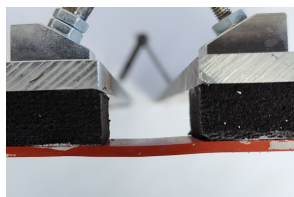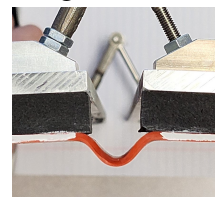
(a) Flat configuration.   (b) Increased inclination between panels.

Figure 2.2: The increased inclination causes the Surface Layer to buckle with no support.

The Surface Layer (SL) is a compliant layer that can handle large strain, while the Stress-relieving Layer provides support to the Surface Layer. The SL is a continuous high strain solid to ensure the OML is continuous, while the Stress-relieving Layer (SRL) is allowed to be discontinuous. The SRL is compressible and resistant to tension, adding impediments to the wrinkling and buckling of the attached Surface Layer. As seen in Figure 2.3, the SRL provides stress relief around the plate edges. Without the SRL, the compliant Surface Layer would have stress concentrations around the edges of the plates. For this design, supersonic airflow is considered for the pressure load, but not the accompanying shear loads. However, these shear loads could be countered with reinforcement in the Surface Layer materials [28]. These layers are to be adhered together, with the Stress-relieving Layer also attached to the panels. The amount of Stress-relieving Layer supporting the Surface Layer (O), the thicknesses of the layers (t), and the amount of pre-strain applied to the Surface Layer ($\epsilon^{(pre)}$) are design considerations (see Figure 2.4). A thicker Stress-relieving Layer will cause the Surface Layer to elongate more when two panels turn away from each other, but will also support the Surface Layer more. The length of SRL overhanging past the panels is determined relative to half the distance between the panels.
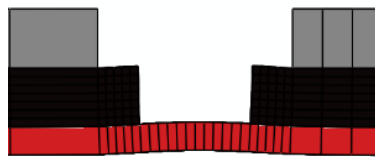
Figure 2.3: The SL has a smoother transition off the panel due to the SRL.
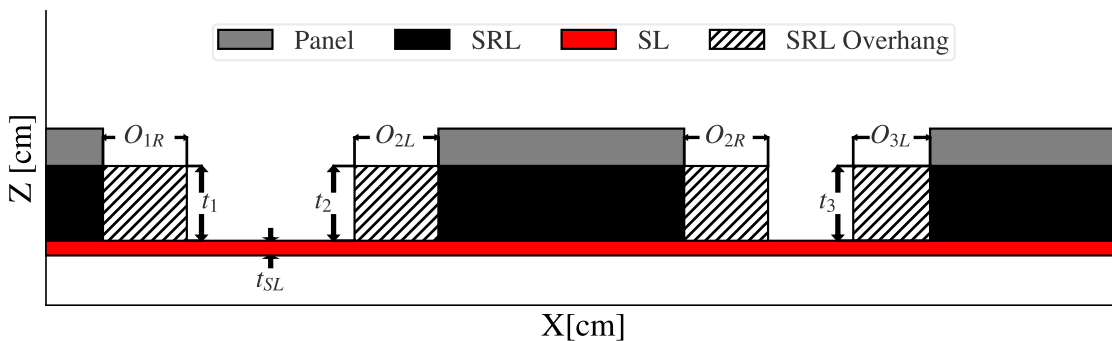
Figure 2.4: SRL and SL design variables schematic

16

2.1.1 Optimization of the Conformal Layer

Optimization of systems with multiple objectives is called multi-objective optimization. Dynamic system analysis using multiple objectives often arrive at superior solutions compared to using a single objective. Figure 2.5 shows an example where, while the overall cost is greater, the multi-objective optimizer found a solution that lowered both costs well. These objectives could be of multiple load states (see Section 1.6) with one performance metric each, one load state with multiple performance metrics [29], and even multiple load states with multiple performance metrics. The convex and concave configurations are both equally likely (see Section 1.6.2) and are required for different environments (see Section 1.3.1), meaning there are at minimum two load states. To guarantee that the conformal layer designs found perform well in both states, only multi-objective optimization will be considered for this work.
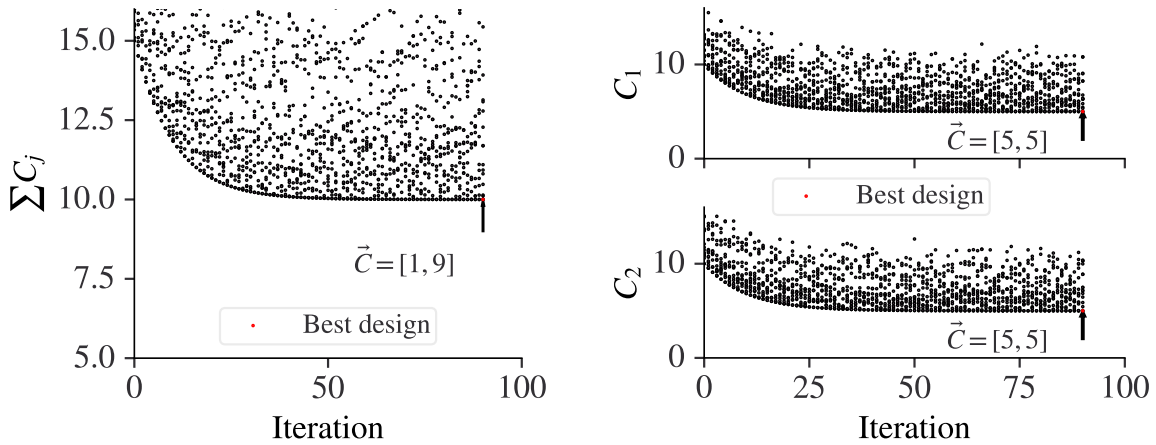
(a) Single Objective Optimization example   (b) Multi-Objective Optimization example

Figure 2.5: Minimization of cost ($\vec{C}$) over iterations example.

The optimization of the conformal layer was performed by using the selected multi-objective optimization method from Section 3.5.4 and optimization cost function in Section 2.1.2 to find the approximate best solution for the design of the three panel structure. To simplify the search, a parametric study (see Section 4.1) was performed to limit the range of designs.

2.1.2   Optimization Cost and Objective Function

The concave and the convex configurations both have a metric to be minimized. As mentioned before, this work will seek to minimize the local mean inclination in flow direction (see Section 1.4) on the Surface Layer. The change in flow direction is linked to the curvature of the surface, which can be described using the principal curvatures κ_1 and κ_2 [30]. The panel system ensures that κ_1 and κ_2 occur along the X and Y axes, respectively. The third axis that measures Z, the height, is used to find κ. For example, the instantaneous curvature along the X-axis is directly related to the second derivative of $Z(X)$, noted as $f(X)$.

$$f(X) = \left(\frac{\partial^2 Z(X)}{\partial X^2} \right) \propto \kappa_1 \tag{2.1}$$

The curvature along the Y-axis, κ_2, does not change in any design. This means that only the curvature along the X-axis, κ_2, is considered. The overall mean curvature along the X-axis is related to the overall mean value of f, as seen in Equation 2.2.

$$\bar{f} = \left(\frac{\int (f(X)) dX}{\int dX} \right) \tag{2.2}$$

Both an increased or decreased inclination and declination are to be minimized. This means that the absolute value of $f(X)$ must be considered. Also, there flat areas over the panels and the possibility of noise from the FEA approximations. Thus, the metric will only be measured when the value is above an expected value, λ, using an indicator function $I(X)$ as shown in Equation Set 2.3.

$$I(X) = \frac{\text{sign}\,(|f(X)| - \lambda) + 1}{2} = \begin{cases} 1, & |f(X)| \geq \lambda \\ 0, & \text{else} \end{cases} \tag{2.3a}$$

$$\bar{f}_2 = \left(\frac{\int (|f(X)| I(X)) dX}{\int I(X) dX} \right) \tag{2.3b}$$

This is now a metric that can be placed into the cost function array.

$$\vec{C} = (\bar{f}_{2,convex}, \bar{f}_{2,concave}) \qquad (2.4)$$

This cost function is used for an example in Figure 2.6a. The grey area is the numerator of $\bar{f}_2$, while the denominator is the length of the dashed line touching the grey area. By only concerning the cost function with these areas, then a possible optimal design would appear as Figure 2.6b.

(a) $C > 0$ (b) $C = 0$
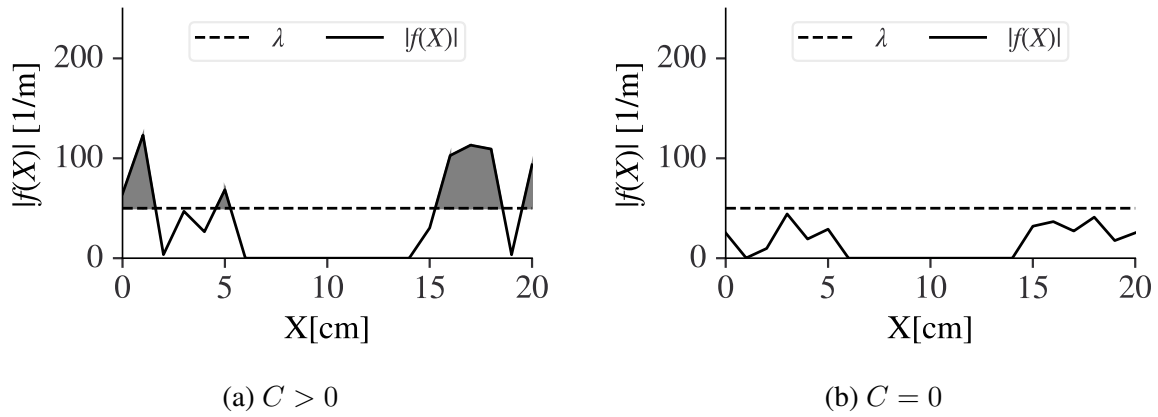
Figure 2.6: Example of the use of the expected noise value, λ.

The value of λ will be determined by measuring the maximum value of noise in an FEA model considering only the pressure load and rounding to the nearest 10 , similar to Figure 2.3.

The objective function is defined as seen Equation 2.5.

$$F = \min([C_{convex}, C_{concave}]) \qquad (2.5)$$

3. ENGINEERING TOOLS

3.1 Finite Element Analysis Tools

3.1.1 Overview

Finite Element Analysis (FEA) is a numerical method to approximate the solution to a mathematical problem. The mathematical problem is approximated by assembling elements from a library of elements [31] into a large numerical problem. The solutions to these problems that can be mapped to a single point are considered to be field variables (e.g., strain). The nodes of an element are where the force and displacement field variables are approximated using the numerical method; elsewhere in the element those field variables are related to the nodes by shape functions. Variables that are integrated over a volume (e.g., energy based on stress and strain) are solved at specific integration points within an element. This numerical method allows for elements with lower-order equations to approximate a mathematical problem of higher-order, allowing computers to efficiently approximate higher analytical problems.

Table 3.1: Comparison between available and applicable FEA software

	Abaqus	SolidWorks	Ansys
Dynamic Analysis	Yes	Yes	Yes
Non-linear Analysis	Yes	Yes	Yes
Complexity[32]	High	Medium	High
Experience	4 years	2 years	0 years

The FEA software options available and applicable to this problem (see Section 2) are compared in Table 3.1. The problem is dynamic and nonlinear due to the materials that may be used for the Stress-relieving Layer (see Section 4.1). Although Abaqus and Ansys are both equally capable of solving the problem, the team is far more experienced with Abaqus. Thus, Abaqus was chosen.

3.1.2 Finite Element Model Interpretation of the Problem

The three-panel system is divided into an aluminum panel, a compressible Stress-relieving Layer, and an incompressible Surface Layer (see Figure 3.1). The hinges are not modelled. Instead, the panels are made to move into the expected configuration with the assumption that sufficiently strong actuators and hinges are available. This is important to recognize, as some designs can create enough concentrated loads to bend the prototype hinges (see Figure 3.3). As the aluminum panel is unlikely to be deflected or peeled from the Stress-relieving Layer, it can be modelled as a shell skin on the Stress-relieving Layer. Similarly, the Surface Layer can also be modelled as a shell since it is incompressible and relatively thin. On the other hand, the Stress-relieving Layer is a compressible material that can be strain rate dependent, thus it must be modelled as a continuum solid. It was assumed that the continuum solid can use one less integration point in each direction as there is no discrete jump in values across a solid element. However, this is tested in Section 6.6 and was shown to be a poor assumption.

Figure 3.1: Panel system, 3 panels in FEA
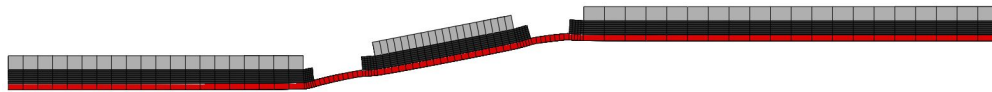
Figure 3.2: Panel system, 3 panels in FEA, concave

Figure 3.3: The first prototype placed on the panel system was enough to bend the hinges.

For the loads, the pressure load is applied exactly as seen in Figure 2.1 up to the X-value of the midpoint of the third panel. As the Surface Layer is forced to compress in areas without support, only tension pre-strain can prevent buckling. The pre-strain on the Surface Layer up to the X-value of the midpoint of the third panel will be applied in the model by using an artificial thermal expansion to shrink the Surface Layer. Thermal expansion is directly related to temperature (T [K]) through the thermal expansion constant ($\alpha[\frac{1}{K}]$) in Equation 3.1. This is used because the rest of the system does not consider temperature, so it will not affect the model other than creating pre-strain. However, in a prototype, the Surface Layer would need to be pre-strained before and during the adhesive bonding process.

$$\epsilon^{(thermal)} = \alpha \Delta T \tag{3.1}$$

The adhesive between the Stress-relieving Layer and Surface Layer is assumed to not fail as the reported shear strengths for applicable adhesive far outweighs the yield strengths of the inner and Surface Layer (see Section 4.1). Thus, the inner and Surface Layer will be tied together (i.e., the degrees of freedom of the nodes in contact are equal). Of the boundary conditions, the least X-value faces will have an X-Symmetry condition while the extrema Y-value faces will have a Y-symmetry condition. See Figures 3.4-3.5 for a detailed drawing.
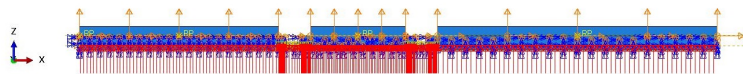
Figure 3.4: A schematic of the loads applied to the three panel system, XZ.
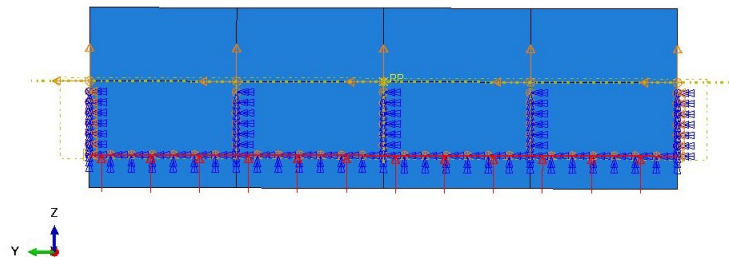
Figure 3.5: A schematic of the loads applied to the three panel system, YZ.

3.1.3 Finite Element Model Parameters

The error in Abaqus' dynamic explicit analysis depends on how many nodes were used to approximate the solution, the size of the intervals of time, and whether the correct element was used [33]. For the thin Surface Layer, a shell element will be used since effects throughout the thickness will be minimized. This means that the outer mold line is not directly measured, instead the bottom surface of the Surface Layer which is assumed to be equivalent. These panels are flat, stiff, all the same thickness, and determine the configuration (see Table 1.1). Thus, the panels will also be shell elements.

Explicit dynamic analysis in Abaqus does not allow shell elements that use second order functions to relate between each other (i.e., quadratic elements). Of the first-order elements, there are fully integrated and reduced integration versions of S4 (i.e., four nodes) and S3. There are special variations of these elements, but they do not apply here (see Table 3.2). Of S4 and S3, S4 elements are a fully integrated finite-membrane-strain elements[34] known to solve bending problems sufficiently well in Explicit dynamics. Thus, S4 is considered.

Table 3.2: The assumptions for special variants of explicit shell elements

Variant	Assumptions
SAX1	Axisymmetric shell (like a wire outer lining)
S4RS	Reduced integration and small strains
S4RSW	Above with warping considered
S3RS	same as S4RS, but with 3 nodes

The shape functions for these elements for in plane values are shown and used in Equation Set 3.2 and in Figure 3.6. The η and ζ act as the non-dimensional coordinates within the element.

$$
4\phi_n(\eta, \zeta) = \begin{cases} (1 - \eta)(1 - \zeta) & \text{if } n == 1 \\[2mm] (1 + \eta)(1 - \zeta) & \text{if } n == 2 \\[2mm] (1 + \eta)(1 + \zeta) & \text{if } n == 3 \\[2mm] (1 - \eta)(1 + \zeta) & \text{if } n == 4 \end{cases} \tag{3.2a}
$$

$$
X(\eta, \zeta) = X_1\phi_1 + X_2\phi_2 + X_3\phi_3 + X_4\phi_4 \tag{3.2b}
$$
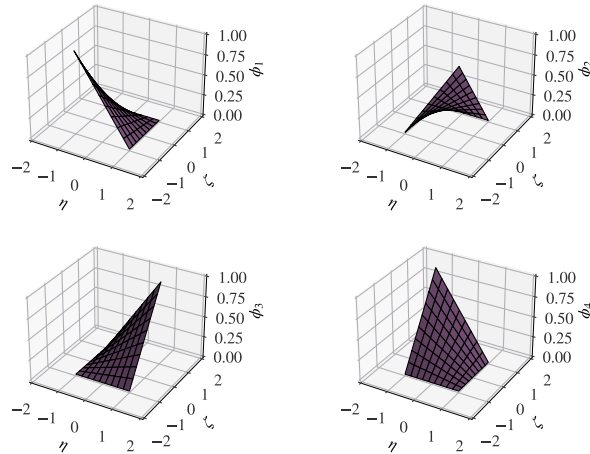
Figure 3.6: Shape Function set 1 of the S4 elements

Table 3.3: Constraints for each bi-linear function

n	$\phi_n(-1, -1)$	$\phi_n(1, -1)$	$\phi_n(1, 1)$	$\phi_n(-1, 1)$
1	1	0	0	0
2	0	1	0	0
3	0	0	1	0
4	0	0	0	1

These bi-linear equations are perfect for interpolating in-plane values like Z and θ, but lack the ability to account for higher-order effects like bending. These out of plane effects are modelled

using higher-order shape functions. Thus, out-of-plane effects are evaluated along one edge using the cubic Hermite spline shape functions in Equation Set 3.3 where η goes from -1 to 1.

$$\phi_{2n}(\eta) = \begin{cases} \frac{H}{2}\left(\frac{1}{2} - \frac{3}{4}\eta + \frac{1}{4}\eta^3\right) & \text{if } n == 1 \\[2mm] \frac{1}{4}(1-\eta)^2(1+\eta) & \text{if } n == 2 \\[2mm] \frac{H}{2}\left(\frac{1}{4}(2 + 3\eta - \eta^3)\right) & \text{if } n == 3 \\[2mm] \frac{1}{4}(-1 - \eta + \eta^2 + \eta^3) & \text{if } n == 4 \end{cases} \tag{3.3a}$$

$$Z(\eta) = Z_1\phi_{21} + \theta_1\phi_{22} + Z_2\phi_{23} + \theta_2\phi_{24} \tag{3.3b}$$

$$f(\eta) = Z_1\frac{d^2\phi_{21}}{d\eta^2} + \theta_1\frac{d^2\phi_{22}}{d\eta^2} + Z_2\frac{d^2\phi_{23}}{d\eta^2} + \theta_2\frac{d^2\phi_{24}}{d\eta^2} \tag{3.3c}$$
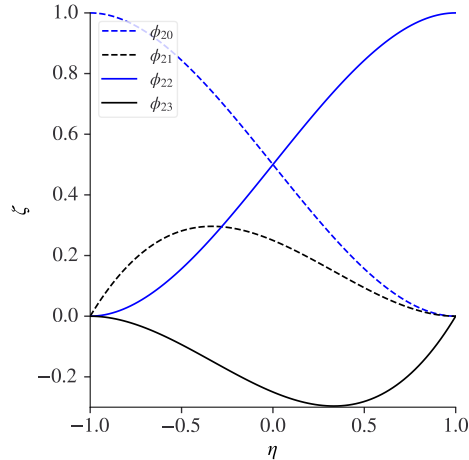
Figure 3.7: Shape Function set 2 used for Z

Similar considerations are made for the continuum solid element. However, there are far more options available in both variants and number of nodes for standard that are lost when using explicit analysis. As the Stress-relieving Layer is effectively a rectangular prism, only rectangular prism-shaped elements need to be considered. Reduced integration is applied to expedite the speed of the model. In order test how much this affects the model, Section 6.6 will explore ten designs from the Pareto frontier (see Section 6.2) with and without reduced integration. This means only the C3D8R elements (i.e., three-dimensional continuum elements with eight nodes and reduced-integration) remain. With 8 nodes, the C3D8R element uses linear assumptions in-element. For standard

analysis, C3D20 is possible. With 20 nodes, the C3D20R element uses quadratic assumptions in-element. C3D8R elements were chosen for the sake of expediting results, although C3D8 would have the most accuracy in explicit and C3D20 would have the best accuracy in Abaqus/Standard (implicit solver).

The meshing of the part is divided into three sections, shown in Figure 3.8. Above the panels, there are $(20, 4, 7)$ elements across the Stress-relieving Layer along the (X, Y, Z) axes respectively. The panels are 2D shells that have $(20, 4)$ elements along the (X, Y) axes. The Surface Layer shell has 20 elements along the X axis and has a mesh size of 1 [mm] along the Y axis. In the second section, where the inner and Surface Layer are attached, the Stress-relieving Layer has $(5, 4, 7)$ and the Surface Layer shell have 20 elements along the X axis. In the third section, where the Surface Layer is free, it has a mesh size of 1 [mm] on both sides. A time scale ($\Delta\tau$) four magnitudes smaller than the total time to complete one configuration transition ($\tau^{(tot)}$) was found to minimize the real run time needed to complete both configurations for a design ($\tau^{(complete)}$) to around 4 to 6 minutes. This mesh size and time scale were determined through the contour plots in Figure 3.9. As the total costs start diverging after 20 elements at the best time scale, 20 elements was chosen. A time scale of five magnitudes less than the total time at 20 elements has the same cost vector as the best time scale.
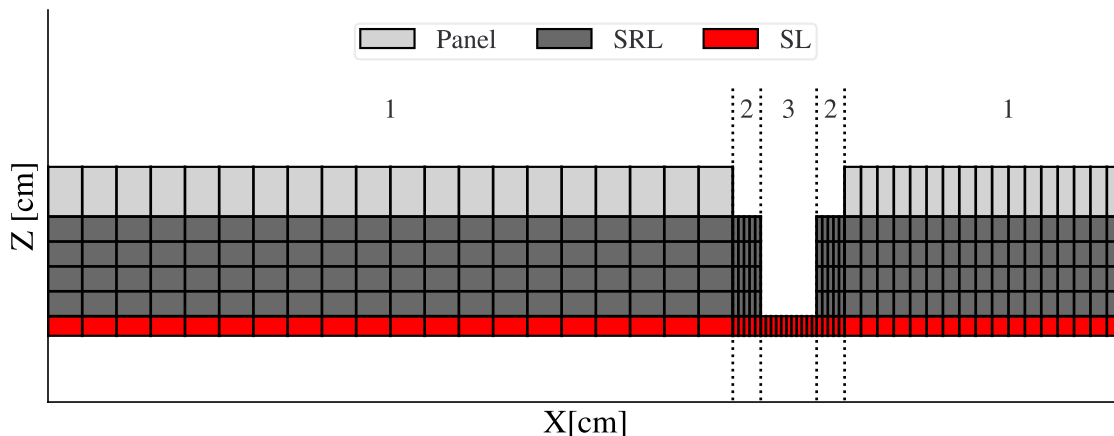
Figure 3.8: The three sections: All attached, SRL and SL attached, free SL.

(a) Time to complete

(b) Sum of costs
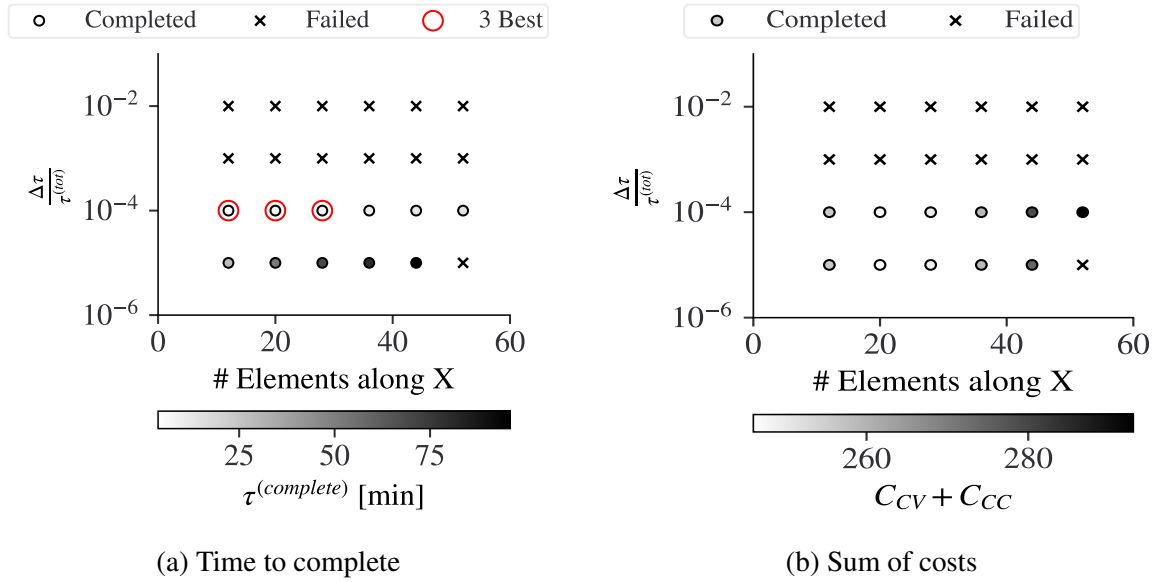
Figure 3.9: Time scale vs X Element Number for the 1st section.

3.1.4 FEA to Cost Function

The cost (or loss) function from Equation 2.4 is integrated into the FEA model by taking the nodal values of Z and θ (small angle approximation, $\approx Z'$) and interpolating values using the shape functions from Equation 3.3. This allows for the values between the nodes to be interpolated as a continuous line, as seen in Figure 3.10a. To take these nodal values, a node set is defined in Abaqus using the known geometry of the design. The OML is on the negative Z normal face of the S4 Surface Layer shells. Thus, any face on the Surface Layer with a negative Z normal is selected. On those faces, all nodes are selected for the node set. The values are then taken over time, but only saved to an excel file when the configuration they are from is as described in Table 1.1.

(a) Interpolation of example node set.

(b) Node set selection from example
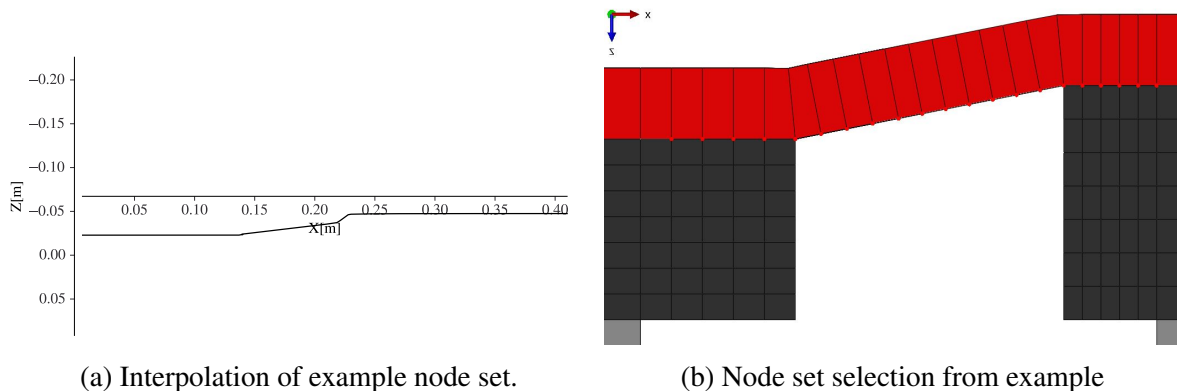
Figure 3.10: High cost design example

27

3.2 Digital Image Correlation

To compare the Surface Layer strain field of a physical sample to that of the Finite Element Analysis model, the displacement of points of interest will be measured. For the measurement, digital image correlation (DIC) via Correlated Solutions software VIC-3D is used. DIC is a non-contact, full-field optical method of measuring the displacement over time of points of interest using images in chronological order [35]. These points of interest are typically speckled black dots onto a non-black background, ideally white, under a white-light. This is because DIC software typically track the change in light intensity of these points of interest over time from various angles to estimate displacement[36].

White flexible acrylic paint by PlaidFX is used to ensure the outer mold line is white while it elongates significantly. However, the paint cannot elastically strain as much as the compliant layer it is attached to, allowing only one cycle of elongation before needing to be replaced (see Figure 3.12). The construction of the sample in Figure 3.11 is seen in Section 3.2.2.

(a) Speckled DIC Sample. (b) The DIC Sample design schematic,XY plane.
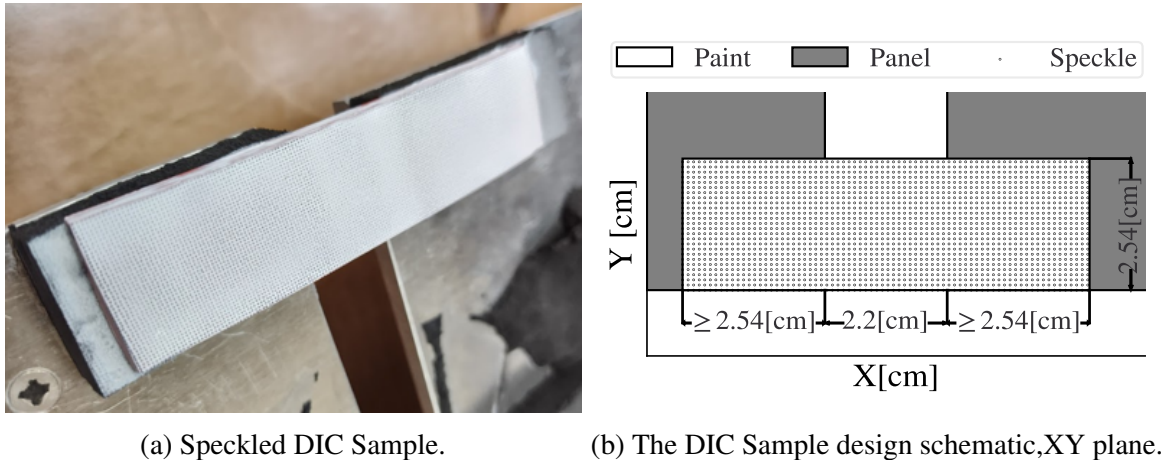
Figure 3.11: DIC Sample.

Figure 3.12: The paint experiences plastic strain after one full cycle.

28

3.2.1 Construction of the Prototype

There are four items in the prototype. These are the panel system, the Stress-relieving Layer (SRL), the Surface Layer (SL), and the adhesive. The prototype starts out with the panel system from Section 1.6.2 already constructed. The SRL and SL are made of the materials selected in Section 4.1.2. The adhesive was selected in Section 4.1.3.

However, the design has the following instructions, no matter the materials:

1. Retrieve the completed panel system, the adhesive, and the materials for the layers.

2. Measure and mark the SRL and SL materials with their desired shapes.

3. Cut out the desired shapes from each material using recommended method.

4. Pre-strain the Surface Layer to the desired amount using grips.

5. Clean all items with near 100% isopropyl alcohol.

6. Ensure all alcohol is removed from the surface.

7. Cover the unshared surfaces with masking tape.

8. Apply primer to the Stress-relieving Layer and panel system planned co-surface.

9. Apply one flat coat of adhesive to the SRL and panel system planned co-surface.

10. Press the layers together lighter than 10% compression of the Stress-relieving Layer.

11. Follow instructions from the manufacturer on curing.

12. Apply the adhesive to the Stress-relieving Layer and Surface Layer planned co-surface.

13. Repeat items 10 and 11 for the Stress-relieving Layer and Surface Layer planned co-surface.

The construction is now complete. Depending on the amount of material applied, the presentation prototype in Figure 1.3 or the DIC testing prototype in Figure 3.13a is now ready to be painted. Some considerations are to be kept in mind, however. In Step 8, the adhesive will fail without primer (see Section 4.1.3). In Step 9, if adhesive goes onto the free surface of the Surface Layer, it will cause significant stress concentrations that will lead to crack development and failure. This is seen in Figure 3.13b.
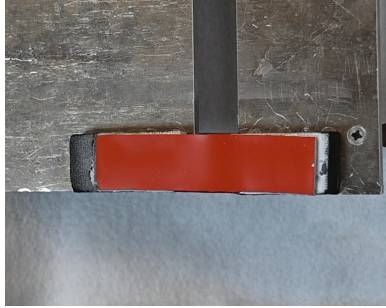
(a) Sample, Digital Image Correlation

(b) Consideration for Step 9.

Figure 3.13: Unpainted DIC sample.

3.2.2 Digital Image Correlation Sample

A sample for three-dimensional digital image correlation is used to validate the results from FEA analysis. The experimental setup in Figure 3.14f includes two Correlated Solutions cameras, a slot to cantilever one panel, and a computer with VIS-3D software. The ideal setup is to record the outer mold line of a sample from one configuration to another. The steps for preparing the digital image correlation (see Section 3.2) sample are as followed .

1. Construct the Figure 3.11b sample following the construction steps from Section 3.2.1.

2. Wear proper personal protective equipment (e.g., Vinyl gloves).

3. Mix water and FX flexible acrylic paint evenly in an unused paper cup with a mixing stick.

4. Construct and attach the Master G22 Airbrush to the Airbrush Depot TC-20 Mini Air Compressor as seen in Figure 3.14b.

5. Cover the areas of the sample not to be painted with masking tape as seen in Figure 3.14c.

6. Apply three layers of adhesive primer selected in Section 4.1.3.

7. Once emptied and dried, fill the paint cup of the airbrush with the diluted paint.

8. Apply two coatings of diluted paint evenly as seen in Figure 3.14d and let dry.

9. Ink the Correlated Solutions 0.013 [in] Speckle Applicator with an Archival Ink pad.

10. Speckle the dried and painted DIC sample and allow the ink to dry.

11. Cantilever the panel system off a flat surface, one panel free to rotate.

12. Orient the 3mm calibration target on top of the sample.

13. Setup the two camera system so that it can clearly see the sample and 3mm target.

14. Take photos of the 3mm target to calibrate the software.

15. Move the panels to the next configuration and take an image every few degrees rotation.

16. Return to the flat configuration.

17. Upload the calibration images and the chronological test images to VIC-3D.
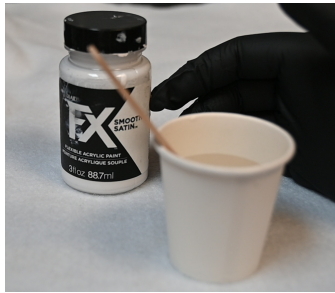
(a) Step 3.

(b) Step 4.
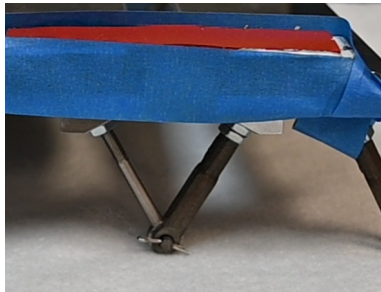
(c) Step 5
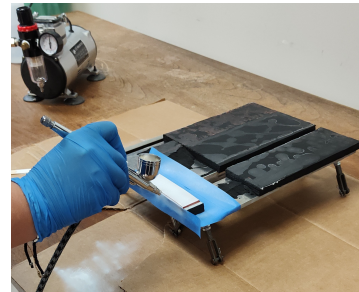
(d) Step 8

(e) Step 9

(f) Step 13.

Figure 3.14: The associated figures for select steps

3.3 Material Testing

3.3.1 Testing the Material Properties

The select materials of a parametric study (see Section 4.1.2) need to be compared through Finite Element Analysis. To perform this comparison, a set of calibration tests for each material were performed. Simple tensile tests and compression tests were used to calibrate stress-strain curves for use in Abaqus. All the materials tested will be sourced from McMaster-Carr[37].

3.3.2 Surface Layer Material Testing

The desired properties for the Surface Layer materials are the stiffness, thickness, and the maximum elongation. There will be a tensile test for these stiffness and maximum elongation, as seen in Figure 3.15. A compression test will not be performed, as these materials will immediately buckle (see Figure 2.1b). To prepare the sample for testing, the inputs from Table 3.4 will be placed into the tensile test machine.
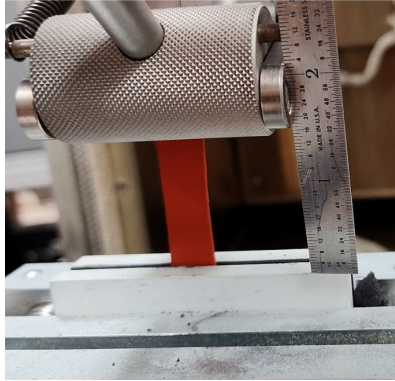
Figure 3.15: Simple tensile test, this one for the Surface Layer.

Table 3.4: The Surface Layer material test setup

Input	Value
$\dot{\epsilon}$	0.25/min
L_0	1"
W_0	0.5"

3.3.3 Stress-Relieving Layer Materials

The Stress-relieving Layer foam-rubber materials are tested in both compression and tension. The tensile test is the same as shown in Figure 3.15. The set-up is also the same except a $\dot{\epsilon} = 0.2[\frac{1}{\min}]$ is used, instead. This test will have the values imported directly into Abaqus. However, most of the Stress-relieving Layer materials reportedly fail quickly in tension, which will also need to be considered.

The compression test will be performed by having the material crushed between two flat surfaces and have the pressure measured by a SHIMPO FG-3003 Digital Force Guage. This is to verify the reported $\epsilon = .25$ compression pressure. The size of this sample is a $1 \times 1 \times 0.5$[in.] rectangular prism. The Stress-relieving Layer materials, unlike the hyper-elastic Surface Layer materials, will cease linear-elastic deformation and begin rapid plastic deformation before the $\epsilon = .25$ pressure [38]. Thus, for an Stress-relieving Layer to not fatigue or tear, the end of the linear-elastic deformation curve must not occur during experimentation.

Figure 3.16: Compression test setup and example

3.3.4 Adhesive Testing

The adhesive test is inspired by the ASTM D1002 standard test [39]. ASTM D1002 is meant to test for the adhesion/cohesion properties (including failure) of an adhesive bonding two metals with a lap shear test. As both of these are hard-to-bond together materials that are not metals, some considerations and modifications are made. This calibration is the most complex experiment of the three, as a sample representative of the prototype must be constructed. To test the adhesives fairly, a common sample will be created and placed into the MTS for lap shear testing. The samples will be made to be $\approx$ 1[in] wide. The SRL was cut to be twice as thick as the SL. There must be a 1[in] long shared surfaces where the adhesive and primer are applied. However, the construction of this component is very sensitive (see Section 3.2.1) as it is similar to the final prototype. Photographs of the process are taken periodically to catch what causes a failure.This test is shown in Figure 3.18 and the strain rate for the MTS is $\dot{\epsilon} = 0.2$[1/min]. If the adhesive can stay completely adhered while other components of the sample yield, then neither cohesive nor adhesive failure need to be taken into account. Otherwise, the cohesive and adhesive failure properties will be required.

Figure 3.17: Creating samples of various adhesion methods between the SL and SRL materials
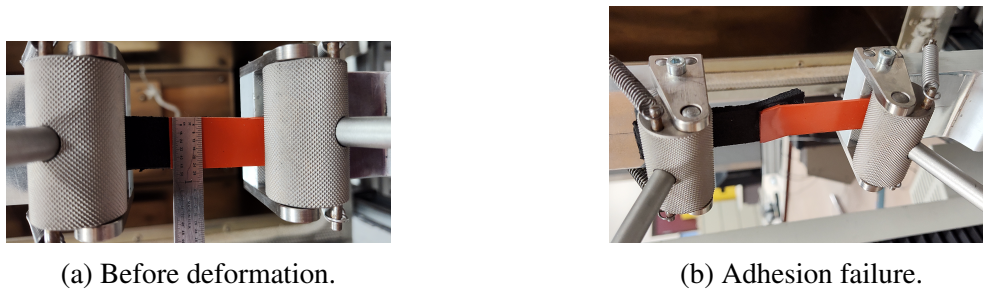
(a) Before deformation.
(b) Adhesion failure.

Figure 3.18: Lap shear test.

3.4 Design of Experiments

The design space can be shrunk significantly by determining the feasible ranges and cost trend lines for each design variable. To measure the trend of each design variable (i.e., influence), samples across the design space must be sampled. Many methods are possible to sample the design space. An LHS divides each DV range into sections and only allows one design to have a value in that section. The DV value in each section is random. When all DVs are non-dimensionalized over their ranges, the section combinations take on the form of local hyper-cubes (e.g., squares, cubes). A FF considers levels (permitted values) in each DV and makes one design for every unique combination of levels [40]. For example, a DV given only three levels and with a range from 0 to 1 will have only $(0, 0.5, 1)$ as levels. Partial sampling of a FF to save on time while maintaining good accuracy is possible. Both FF and LHS are space filling, but the LHS has resilience as a failed sample in a local hyper-cube can be overwritten with a new random sample in the local hyper-cube.

Generally, an LHS is not enough to determine influence as only one design will be attempted for each local hyper-cube. However, a simplification for this work is that, for each DV, there are ten levels between and including the minimum and maximum value range as seen in Equation Set 3.4. This means that there are 10^8 unique level combinations. This work will use a normal LHS to generate unique designs with DV values between the levels, then round them to their nearest permitted value as a modified LHS. An example of this is seen in Figure 3.19a. Failed or repeated designs will be overwritten by a new design connected to the same local hyper-cube if possible.

$$\vec{D} \propto (O_1, O_2, O_3, t_1, t_2, t_3, \epsilon^{(pre)}, t_O) \tag{3.4a}$$

$$D_i : \{D_i \in \mathbf{Z} | 0 \le D_i \le 9\} \tag{3.4b}$$

$$\text{Example: } O_1(D_1) = \begin{cases} O_1^{(min)} & D_1 = 0 \\ O_1^{(max)} & D_1 = 9 \end{cases} \tag{3.4c}$$

35

As an example for the usage, the cost functions $A(X, Y) = (5 - X)(2 + Y)$ and $B(X, Y) = 2^{-X}$ are used with $(X, Y) : \{(X, Y) \in \mathbf{Z}|(0, 0) \leq (X, Y) \leq (9, 9)\}$. The design space is explored using both 100 sample FF and the 50 sample modified LHS in Figure 3.19b. Y clearly has a linear relationship with A, no relationship with B, and can be removed as a DV and set as a parameter. If the objective function sought to minimize $|A(X, Y)|$, then this would mean setting $Y = 0$. With only X as a DV, the exploration and optimization of an objective function is much simpler. The modified LHS and the FF found similar trends.

(a) LHS points rounded to nearest levels. (b) FF vs mod. LHS
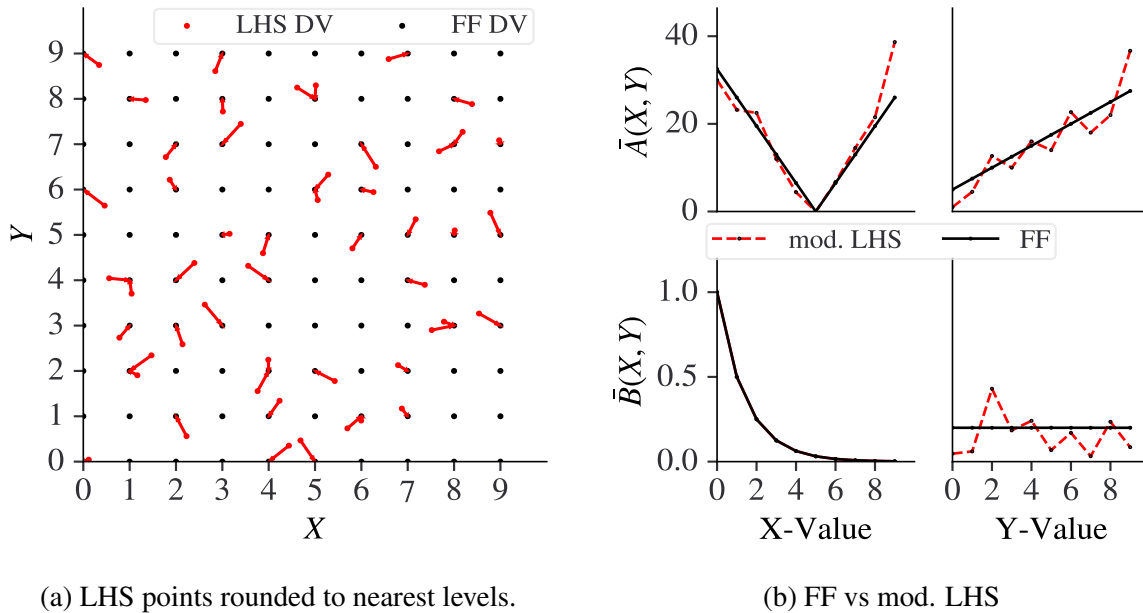
Figure 3.19: A modified LHS is compared to a FF in plotting trend lines.

3.5 Optimization Methodology

The optimization of the conformal surface can take into account the topology, material properties, sizing, and shaping the structure. The mechanical properties of each material will be determined by parametric studies in Section 4. The shaping of the structure is directly tied to the sizing of parts of the structure, as seen in Figure 2.4. The sizing and pre-strain of the structure is controlled by an array of design variables. The arrays of design variables are generated by and their associated outputs are placed into a genetic algorithm wrapper utilizing NSGA-II (see Section 3.5.1) to generate new generations of designs. This leaves topology optimization of the sized and shaped structure. When performing topology optimization, two methods were considered. The first method is built into the Abaqus optimization module, Tosca Structure, and the second is an L-system approach to topology optimization called SPIDRS. Both were were abandoned in the current work, as explained in Section 3.5.4.

3.5.1 NSGA-II

After determining the important variables and their ranges, the array of design variables can then be placed into any optimizer. For example, the non-dominated sorting genetic algorithm, NSGA-II, is well suited to multi-objective optimization [41]. A design ($\vec{D}$) dominates ($\prec$) another design if both cases in Equation 3.5 are satisfied. The non-dominated solutions form the approximate Pareto frontier. The non-dominated solutions are of the first front, the solutions that are only dominated by the non-dominated solutions are of the second front, and so forth. NSGA-II uses all of the first two fronts and a select number of the third front to parent the next generation of samples. In each front, solutions are ranked according to their crowding distance. The NSGA-II version used is from the open source python framework, pymoo[42].

$$\vec{D}_1 \prec \vec{D}_2 \text{ if both} \begin{cases} C_i(\vec{D}_1) \leq C_i(\vec{D}_2) & \text{for all } i \\ C_i(\vec{D}_1) < C_i(\vec{D}_2) & \text{for at least one } i \end{cases} \tag{3.5}$$

The utopia point is a hypothetical design with a cost vector, $\vec{C}_U$, composed of the minimum

37

value for each cost as seen in Equation 3.6.

$$\vec{C}_U = (\min(C_{CV}(\vec{D}_i)), \min(C_{CC}(\vec{D}_j))) \tag{3.6}$$

The design with the smallest vector from the utopia point ($\Delta \vec{C}$) is considered the best non-dominated design. The justification for using this utopia point to design cost vector rather than the origin is that, while hypothetically possible, all cost vector $\vec{C}$ components are not assumed to have a design with a minimum of zero. This means that the origin is not assumed to be feasible.

$$\Delta \vec{C}(\vec{D}_j) = \vec{C}(\vec{D}_j) - \vec{C}_U \tag{3.7}$$
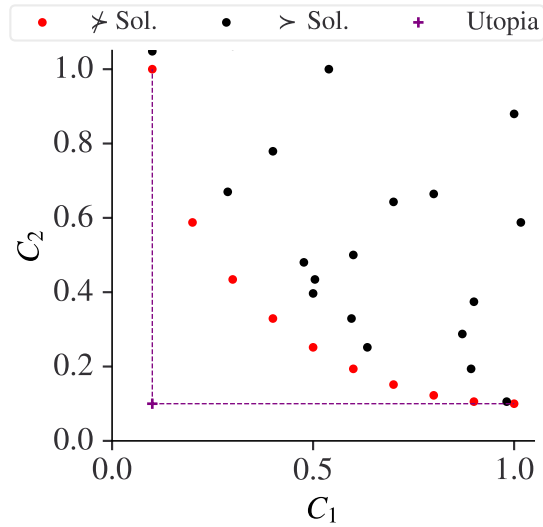
Figure 3.20: An example front of non-dominated solutions.

3.5.2 Method: Tosca Structure With NSGA-II

Tosca Structure is a modular system for non-parametric structural optimization. With SIMU-LIA Tosca Structure, it is possible to carry out topology and shape optimization on a model [33]. For topology optimization, Tosca uses the Solid Isotropic Material with Penalization (SIMP) material distribution interpolation scheme [43]. The relative density parameter of each element in the Abaqus model ranges from 0 to 1. The removed material is assumed to be coalesced into a void inclusion, allowing the material properties to be homogenized. SIMP assumes that the material properties are lost uniformly in all directions. User input determines at what density relative to the no-void density (ρ_0) the elements are deleted. This can be seen in Equation 3.8. The penalization factor (p) determines how much a loss of material means in the loss-in-strength. An anisotropic material will have their direction-based property relations applied afterwards.

$$E = E_0 \left(\frac{\rho}{\rho_0} \right)^p \tag{3.8}$$
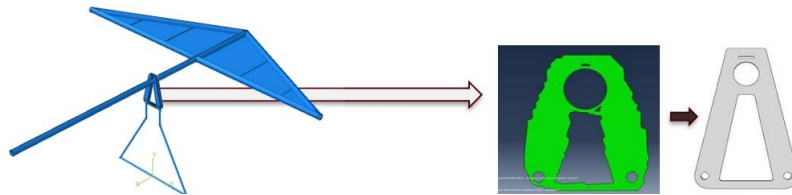
Figure 3.21: A hang glider bracket topologically optimized, then simplified.

A different structural problem was solved using Tosca. In this problem, a hang glider (see Figure 3.21) was shaped and sized according to an array of design variables, with each new design having a load-bearing joint bracket. Sometimes the bracket accommodated both the crossbar and the keel of the hang glider. This load-bearing bracket was then topologically optimized to minimize stress and strain. The resulting mass of the entire construction was the main cost metric of the design (subject to stress constraints). The topology optimization for each design of this part was

performed in Abaqus and a genetic algorithm in a wrapper was used to select new designs.

Because of this experience, the initial research into the design and optimization of the conformal surface layer was done with Tosca and NSGA-II. In this initial research, the conformal layer was a completely solid silicone rubber sheet attached to analytically rigid panels as seen in Figure 3.22. These panels were connected by hinges. The single objective function in TOSCA was to minimize the mean distance between the OML nodes and the desired OML surface $Z_d(X, Y)$, as expressed in Equation 3.9, unlike the current goal to achieve a smooth outer mold line.

$$F^{(old)} = min(|Z(X,Y) - Z_d(X,Y)|) \tag{3.9}$$

(a) Isometric

(b) Schematic
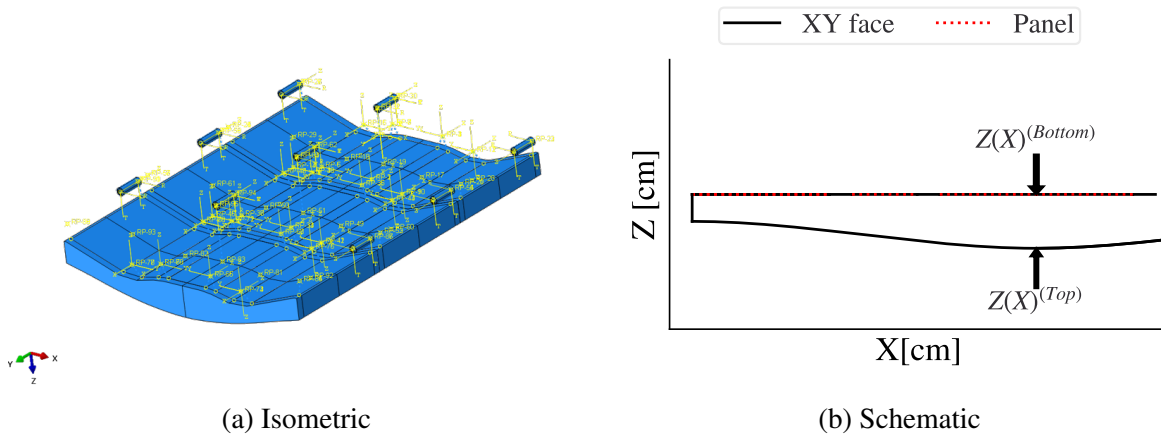
Figure 3.22: The initial research model using Tosca

This model first included actuating shape memory alloy torque tubes to actuate the hinges of the first and fifth panel and linearly actuate the center panel. However, the torque tubes were removed and the panels were made to rotate via boundary conditions placed on their hinges. A 0.5 [psi] pressure load was applied to the outer mold line. To define the conformal layer, the bottom surface was defined as linearly interpolating between the panels, the top surface held the outer mold line and was defined using the cubic shape functions from Equation 3.3. The array of design variables in the wrapper around Abaqus included the $Z^{(Top)}$ and $Z'^{(Top)}$ (small angle approximation, $\approx \theta^{(Top)}$)

40

values at discrete points at $\tau = 0$ [s] to define $Z(X)$, angular displacement of the hinges, and the linear Z displacement of the center panel.

As seen in Figure 3.23, a single half panel with hinge example was optimized. A Y-symmetry boundary condition was placed on the leftmost face, but not the rightmost. The rightmost faces were free to deform in this test. The designs took around 10 minutes to complete, with the large majority of this time being from topology optimization. When expanded into a 5 panel model, the time to complete reached up to 30 minutes per design. This was not acceptable due to time constraints during the project.

Also, the objective function for Tosca must be defined in Abaqus using design responses (e.g., stress, strain). The metric used in Equation 2.3b is not easily transferred due to this.

(a) Initial   (b) Actuated
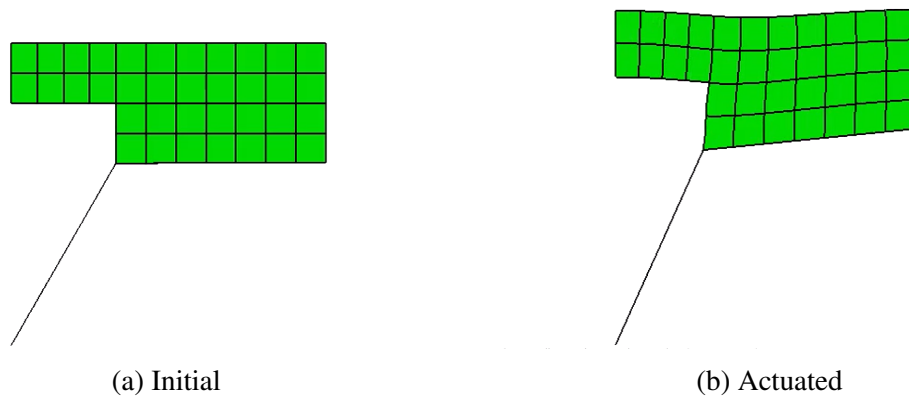
Figure 3.23: The rotation about a stiff hinge in the initial model.
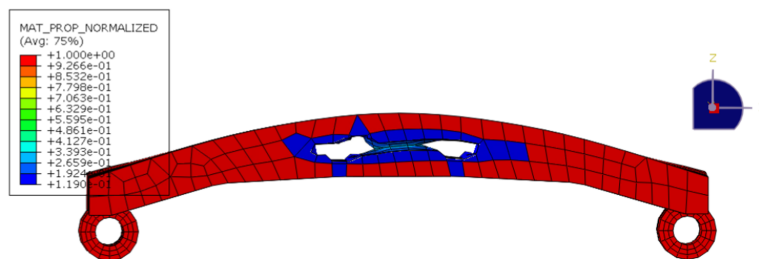
Figure 3.24: Early topology optimization attempt on 5 panels

3.5.3 Method: L-system SPIDRS With NSGA-II

Leaving the built-in Abaqus optimization environment entirely, we can use only optimization tools in a wrapper. One example is SPIDRS, shown in Figure 3.25. SPIDRS for Abaqus is an L-system approach that creates nodes and their relations through modifying a string of commands with a set of commands [44]. The commands move the titular "spider" around and create nodes and/or relations between nodes. This string of commands describes the topology, sizing, and/or functionality of elements within and attached to the structure created via the array of design variables. This graph based method is a topology optimizer that grows in complexity as the command string increases in length [44]. For Abaqus, this method is used to create an extruded shell structure via 2D drawing attached to a design shaped and sized by the array of design variables [45]. The 2D shell structure version of this method takes advantage of the auto-trim feature of Abaqus. The relations could even be for a linked set of nodes to form solid structures. Modifications to SPIDRS would allow for even more types of connections (e.g., springs and hinges). Overall, SPIDRS is a very useful topology optimization method that could reinforce another method, but attempts to integrate the method into this structure were fruitless due to both inexperience with the method and time constraints.

(a) Solid element creation.

(b) SPIDRS refining a design (unextruded).
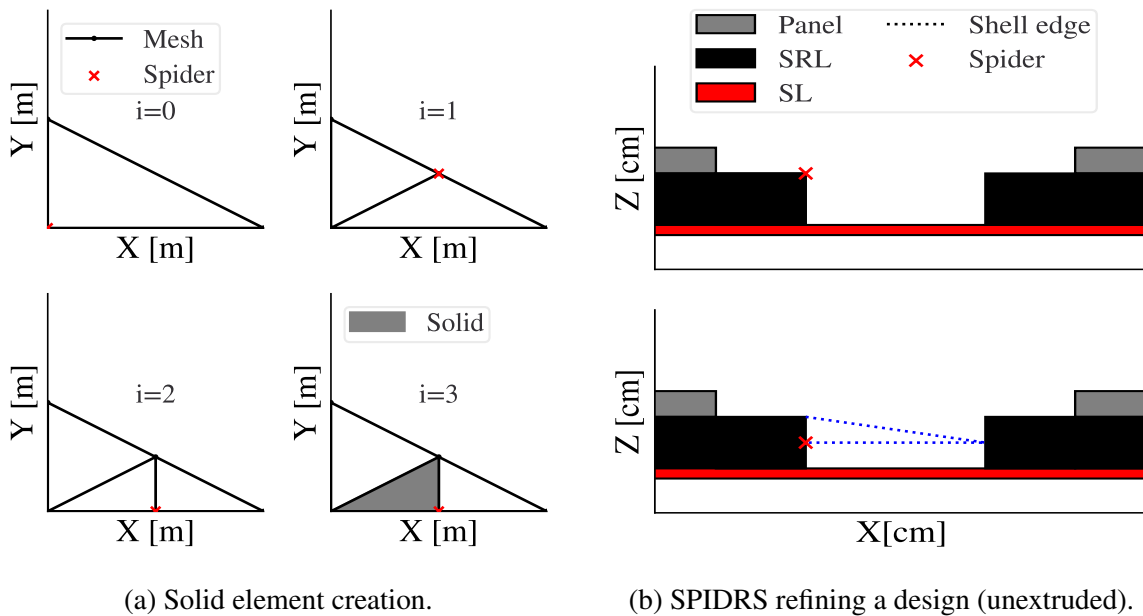
Figure 3.25: SPIDRS refining designs with solid elements and shell edges.

3.5.4 Method: NSGA-II Only

This design will have a high computational cost per run (due to strain rate dependency and large strains) and a similar design to the optimal design will need to be constructed for adequate validation of the model. While topology optimization would be beneficial for the design of the Stress-relieving Layer, the amount of time required to complete the topology optimization greatly increased the total run time. The run time for creating and running a design without topology optimization was shown in Figure 3.9, which is about seven times less run time per design. Additionally, creating a physical validation model sample with a topologically complex design would complicate fabrication.

Thus, instead of performing topology optimization, it was determined to only perform optimization with a python wrapper around Abaqus of NSGA-II from pymoo. The Abaqus model will utilize an array of design variables ($\vec{D}$) inputted from the wrapper that relate to the size and pre-strain of the model alone (see Figure 2.4 and Equation 3.4). The model will then undertake the kinematic paths between configurations from Table 1.1 with the boundary conditions, element types, and element sizes from Section 3.1. The node set selected via the method in Section 3.1.4 will be used to output the displacement, stress, and strain fields for use in the cost function from Equation 2.4. These cost from each generation of designs will be inputted into the NSGA-II genetic algorithm, which will generate a new set of designs to test and rank. Two sets of optimization will be performed. Each set of optimization needs to be robust, thus over 1000 designs (minimum 20 generations of 50 designs) will be tested per set. However, the topology optimization methods could be applied on the top 100 designs in future work to reinforce the top designs from the chosen optimization method. With enough computation power, the method described in 3.5.2 could even be performed in parallel.

4. DESIGN EXPLORATION

4.1 Parametric Studies

4.1.1 Surface Layers Material Selection

The Surface Layer will be a hyper-elastic material, which can be modelled using hyper-elastic constitutive models. The data points of a tensile test are inputted into the Yeoh hyper-elastic model in Abaqus. There are many available materials and they all have different maximum elastic strains and availability. For example, thermoplastic polyurethane (TPU) and silicone rubber are both hyper-elastic materials that can have maximum elastic strains beyond 200% strain, but TPU is not available in solid sheet form from McMaster-Carr [46]. Thus, silicone rubber was selected. There are many varieties of silicone rubber, from 40A to 70A Shore Hardness, with the lower stress at the same strain materials generally having a lower hardness [37, ID:1460N33]. As we require lower stress-strain curves, the 40A silicone rubber was selected. The material properties of the silicone rubber placed into the Abaqus file were derived from a tensile test as seen in the Figure 4.1. This test was not enough to show the true extend of the hyper-elastic effects, as the test only went up to 200%. A short experiment to determine where the reported 5.8 [MPa] tensile stress at break occurs revealed the strain at break to be $\epsilon_{11} \approx 3$. This reveals a large hyperelastic effect, although more tensile testing should be performed in future work for more accurate modelling.
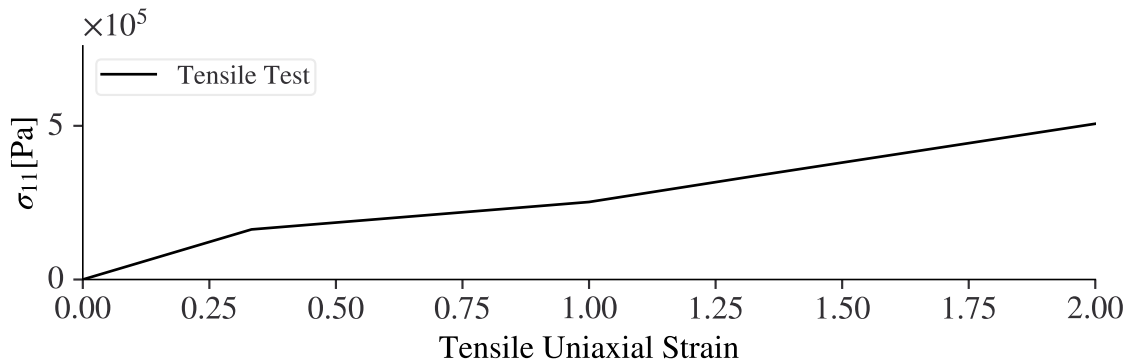
Figure 4.1: Tensile test for the rubber

4.1.2 Stress-Relieving Layer Material Test

In order to select the material, a simple FEA model was used to simulate the various material properties based off of one test sample of a similar foam. There is a 0.5 [psi] load upon the outer mold line (OML). The SRL simulated material testing was between three materials. The different thicknesses within the ranges determined by Section 4. These simulated foams are assumed to follow the stress strain relationship from the following test on a sample of foam [37, ID:86375K111], just made to fit based on their reported uniaxial compression pressure at 25% uniaxial strain. Some of the foams tested in the model were low density. Thus, they were all modelled using the low-density foam model in Abaqus. However, it was found after the completion of this work that there is no significant strain rate dependent effects at our current time scale [47]. The foam model could be set to hyperfoam (similar load path, but no strain rate dependency) in future work. This material test was done with a previous method of creating the cubic interpolation of $Z(X)$ using three points, but used the same cost function with $\lambda = 0$.
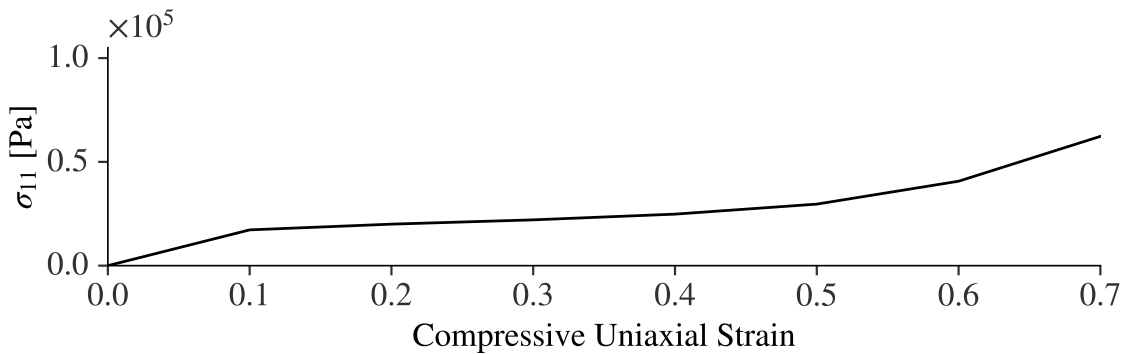
Figure 4.2: Compression test
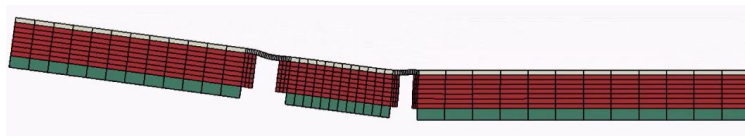
Figure 4.3: Simple concave test used for the SRL materials

The overview of these simulated tests is seen in Table 4.1. Foam 0 [37, ID:8643K544] and Foam 1 [37, ID:8647K201] had 100 modified LHS overhang designs with 5 permitted overwrites each for four different thicknesses, but none completed. Foam 2 [37, ID:8647K301] managed to have converging solutions and even create the design in Figure 4.3.

Table 4.1: SRL material selection table, 100 samples runs each row.

Thickness [in.]	Foam	PSI @ 25%	Best $\vec{C}$ [m^{-1}]
0.25	0	0.6	NONE
0.325	0	0.6	NONE
0.5	0	0.6	NONE
0.25	1	4	NONE
0.325	1	4	NONE
0.5	1	4	NONE
0.75	1	4	NONE
0.25	2	7	(196, 223)
0.325	2	7	(329, 365)
0.5	2	7	(444, 400)
0.75	2	7	(494, 574)

4.1.3   Adhesive Testing

The FEA model assumes perfect adhesion, but the Stress-relieving Layers (SRL) and Surface Layers (SL) are made of hard-to-bond together materials. These hard-to-bond materials require particular methods to adhere together. For the materials selected, two adhesives from Loctite were tested with and without the Loctite SF 770 primer [37, ID:66205A24] (see Figure 3.17). The results can be seen in Table 4.3 and Figure 4.4.

Of all the materials, the Stress-Relieving Layer (SRL) fractured the most often once at least two coats of primer were applied while the adhesive failed in adhesion when there was no primer. Neither the Loctite 499 nor Loctite 422 performed remarkably better than the other without primer. As 499 and 422 are similar in price, but 499 performed better, 499 was chosen. However, an interesting consideration must be taken into account: the adhesive and primer together are able

adhere strongly to the rubber. The adhesion is so strong that attempts to remove the rubber from the adhesive through peeling causes the fracture of the rubber (see Figure 4.4b).

Table 4.2: Adhesive Material test results

Material	Reported shear strength	Reported peel strength
Loctite 499 [37, ID:74985A57]	$2,610$ lbs./sq.in.	2 lbs./in. width
Loctite 422 [37, ID:74985A67]	$2,610$ lbs./sq.in.	2 lbs./in. width

Table 4.3: Adhesive Material properties, reported

Adhesive	Outcome with 770?	Outcome without 770?
Loctite 499	SRL fractures	Adhesion failure, SL
Loctite 422	SRL fractures	Adhesion failure, SL
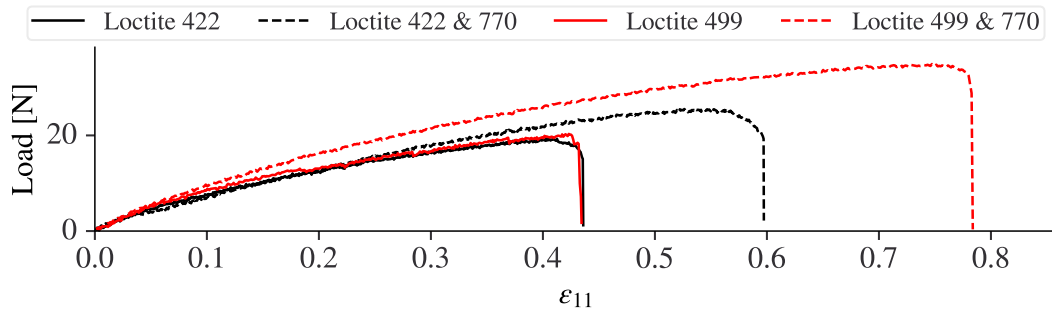
Figure 4.4: Lap shear test results, 0 or 2 coats of Loctite 770
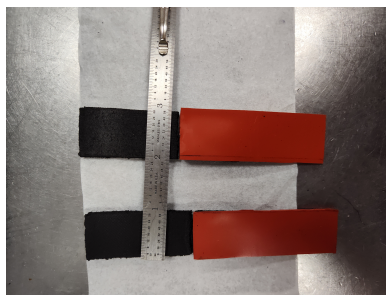
(a) These samples fractured the SRL first.

(b) SL fractures from peeling.

Figure 4.5: The adhesion failure does not occur with enough primer.

4.2 DOE Setup

4.2.1 Array of Design Variable Sampling

A modified LHS sampling will be performed to produce the arrays of design variables. There will be ten levels for each design variable (D_i) according to Equation 3.4 and Figure 2.4. There will be 200 samples. ΔX is the distance is between panels in the flat configuration. These are the limits selected for the LHS:

1. Overhang: $(O_1, O_2, O_3) \propto (D_1, D_2, D_3)$
   $O_i : \{O_i \in \mathbf{R} | 0\% \leq \frac{2O_i}{\Delta X} \leq 80\%\}$

2. Thicknesses, SRL, panel 1: $t_1 \propto D_4$
   $t_1 : \{t_1 \in \mathbf{R} | 0.1[\text{in}] \leq t_i \leq 1[\text{in}]\}$

3. Thicknesses, SRL, panels 2 & 3 $(t_2, t_3) \propto (D_5, D_6)$
   $(t_2, t_3) : \{(t_2, t_3) \in \mathbf{R} | .1[\text{in}] \leq \text{abs}((t_2, t_3) - t_1) \leq .4[\text{in}]\}$

4. Pre-strain: $\epsilon^{(pre)} \propto D_7$
   $t_{SL} : \{t_{SL} \in \mathbf{R} | 2/32[\text{in}] \leq t_{SL} \leq 4/32[\text{in}]\}$

5. Thickness, Surface Layer: $t_{SL} \propto D_8$
   $\epsilon^{(pre)} : \{\epsilon^{(pre)} \in \mathbf{R} | 0\% \leq \epsilon^{(pre)} \leq 80\%\}$

4.2.2 Loads, Constraints, and Boundary Conditions

The loads for the DOE are the same to the current optimization (see Section3.1.2) work. The configurations are the same, as well. If the design violates a constraint or fails to converge, it will be overwritten the next successful run. These constraints are noted in Table 4.4. Boundary conditions for this model are the same as described in Section 3.1.2.

Table 4.4: Constraints and their purpose.

Variable	Constraint	Purpose
$Z(X)\|_{OML}$	One solution	The OML should never fold over itself or tear
$\epsilon_{11}(X)\|_{OML}$	$\epsilon_{11}(X) < 2.0$	Material failure and fatigue are considered
σ_{mises}	$\sigma_{mises} < \sigma_{mises,yield}$	Material failure is considered

Of the overall results of 200 designs created by the modified LHS, 52 designs had the average cost less than 3000 for both configurations. As seen in Figure 4.6, every design variable was influential for at least one configuration.
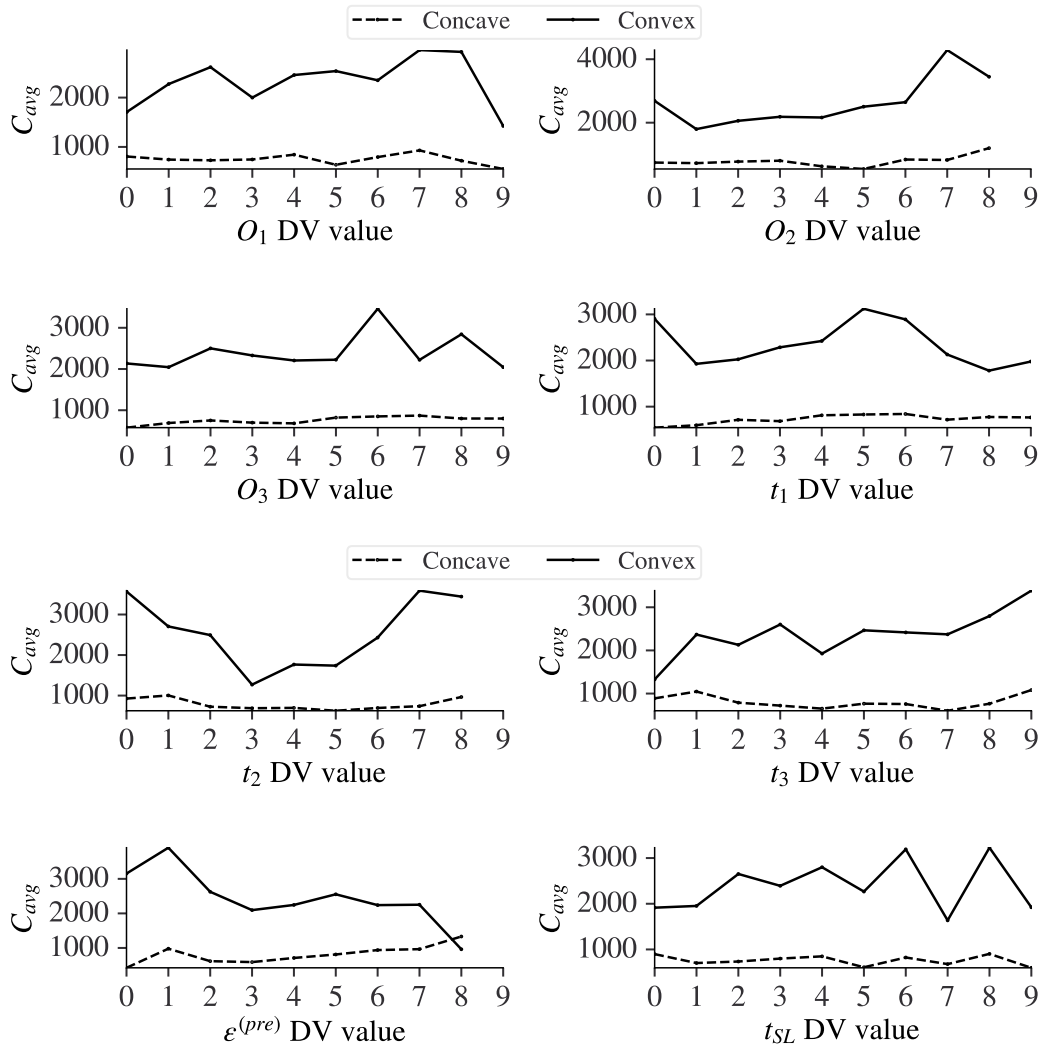
Figure 4.6: DOE Results for Concave (CC) and Convex (CV) configurations

However, no variable had a flat curve in both configurations, unlike in Figure 3.19b. Thus, no design variable can be excluded, though they can be limited. This also shows that the concave configuration usually has a lower cost (on average) than the convex configuration. Those that failed to numerically converge during an Abaqus run consistently had values two O_i above 50% overhang. The values of thickness mainly concerned the convex configuration. The thickness of the second panel would perform better if they were closer to the first panel, $D_5 \approx 5$ and seem prefer to be thinner. Although it seems thinner Stress-relieving Layers performed well, it is only after around $t_1 = 0.2[in]$ that more than a few designs survive. The same is true with overhang. Designs often failed to numerically converge when $(D_1, D_2, D_3) \geq 3$, or the overhang was less than 27%. Pre-strain greatly improved the effectiveness of the concave configuration, but the convex configuration worsens after $D_7 \geq 3$. The pre-strain reduces costs more in the concave than it increases costs in the convex, however. While no design in the modified LHS converged when $D_7 = 9$, the trendlines show that more pre-strain (if possible) is preferable overall. The thickness of the Surface Layers had a complex relationship with the output variables, so the limits shall remain the same.

The results of DOE and the sizing of the available material (see Section 4.1) reveals the following limits should be in place for later optimization:

1. $O_i : \{O_i \in \mathbf{R} | 30\% \leq \frac{2O_i}{\Delta X} \leq 84\% \}$

2. $t_1 : \{t_1 \in \mathbf{R} | 0.25[in] \leq t_i \leq 1[in] \}$

3. $(t_2, t_3) : \{(t_2, t_3) \in \mathbf{R} | -.2[in] \leq (t_2, t_3) - t_1 \leq .2[in] \}$

4. $t_{SL} : \{t_{SL} \in \mathbf{R} | 2/32[in] \leq t_{SL} \leq 4/32[in] \}$

5. $\epsilon^{(pre)} : \{\epsilon^{(pre)} \in \mathbf{R} | 0\% \leq \epsilon^{(pre)} \leq 84\% \}$

5. VALIDATION

5.1 DIC Measurements

The DIC Camera setup (see Section 3.2) is used to capture images of a two panel "flush" (i.e., $O_i = 0$) design with an SRL equal height of 0.5[in] between two configurations. The first configuration was to be flat and the second configuration was very declined. A small wooden spacer was made using the FEA model in these configurations to ensure the positions were rather flat and not too declined ($\epsilon_{11} < 2$), respectively. The FEA model would be made to move as shown in Table 5.1. These panel motions are from the DIC measurements, for fair comparison. During the image taking process, the plates were moved by hand into each configuration.

Table 5.1: Position values from DIC for the two panel "flush" design two configurations.

Configuration	panel	$\vec{X}^{(Top, middle)}$[cm]	$\vec{n}$
0	1	$(6.7, 0, 0)$	$(0, 0, -1)$
0	2	$(18.8, 0, 0.009)$	$\approx (0, 0, -1)$
1	1	$(6.7, 0, 0)$	$(0, 0, -1)$
1	2	$(19.8, 0, 1.2)$	$(.189, 0, -.982)$
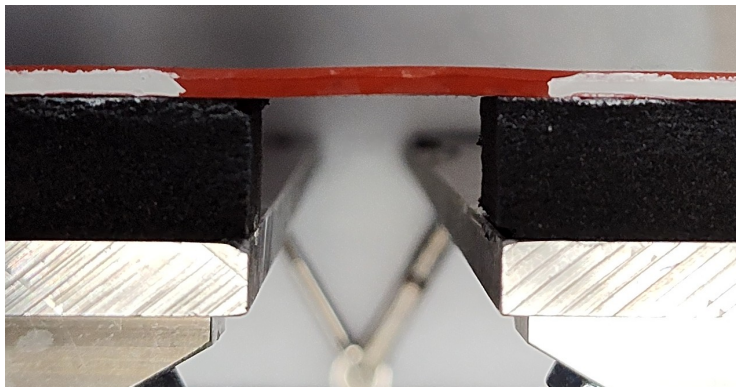
Figure 5.1: The "flush" configuration with equal height, two panels.

The DIC measurements over time are important for the validation of the FEA model. The second configuration's data is shown in Figure 5.2. The DIC measurements found that the first configuration was not exactly flat, likely due to the fact the motion was controlled by hand. The panel motions were then replicated onto Table 5.1 and used to make an FEA model.

(a) ϵ_{11} Measurements, 2D

(b) ϵ_{22} Measurements, 2D
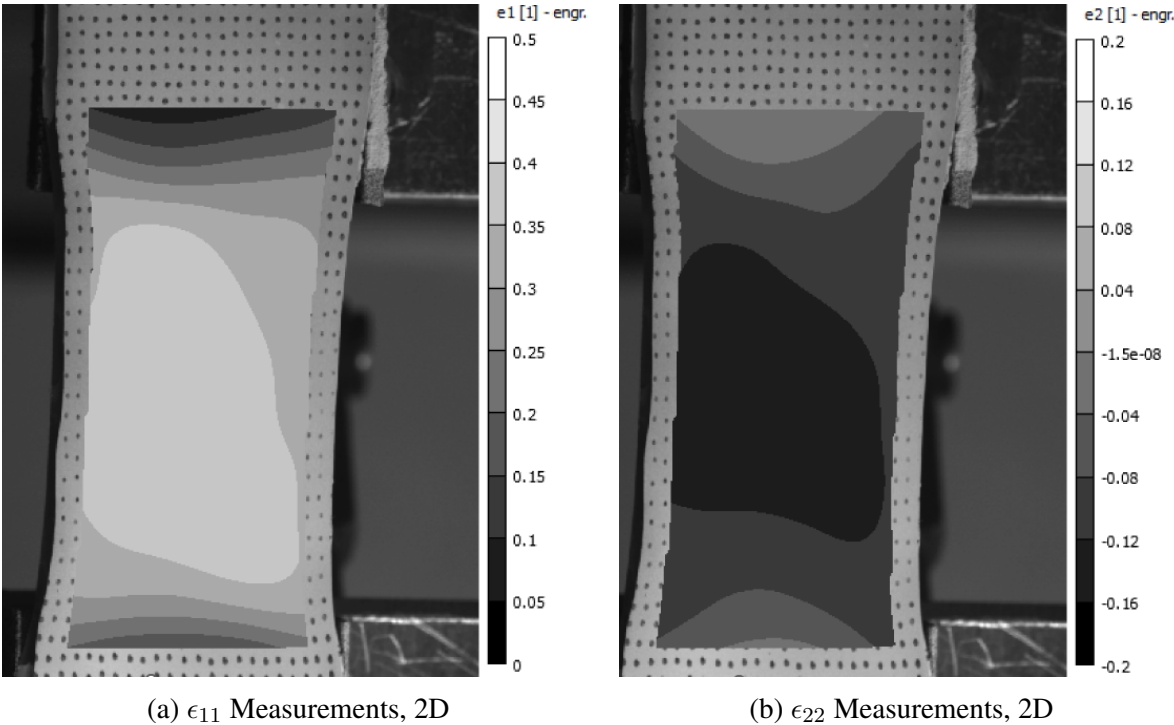
Figure 5.2: DIC measurements at maximum strain configuration

However, these tests were not perfect. During the sample creation process (see Section 3.3), there was a small unglued surface as seen in Figure 5.3a. Section 5.1.1 will explain the mitigation strategy for this error.

5.1.1   Comparison to FEA

DIC measurements were used to validate the FEA using configuration values from Table 5.1. There are no external loads or boundary conditions other than the panels moving, unlike the DOE and Optimization models, to simulate the DIC sample. The Surface Layers is also modelled as a full 3D continuum element, to capture the strain of the OML directly.

However, there were numerous issues that complicated this study. First, the DIC measurements had to be aligned with the FEA values, as the camera placement was not perfect. This was remedied by taking known reference points that exist on the FEA model and DIC sample to create axes for each and transforming the DIC mesh to line up both sets of axes. The FEA and DIC undeformed nodal coordinates are shown in Figure 5.3. The DIC coordinates were shifted in Y for visual clarity.
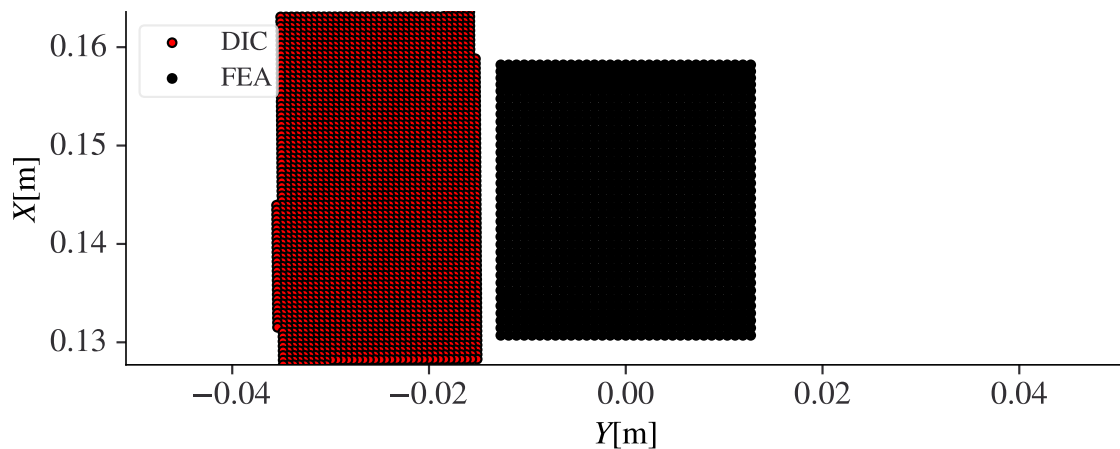
Figure 5.3: DIC and FEA data points in the XY plane

(a) DIC Sample observation.   (b) FEA Interpretation.
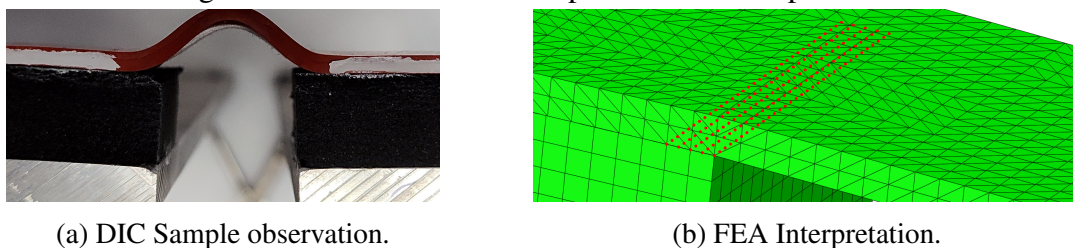
Figure 5.4: DIC sample errors informs the FEA model. Red nodes are in frictionless contact.

Second, there were unglued areas in the physical sample, which was then modelled in FEA as well. This is shown in Figures 2.1b and 5.3a. This was required another modification to the FEA validation model. The measured X axis length of the unglued surfaces were roughly $3[\text{mm}]$ on the bottom side and 4 [mm] on the top side. The size of these unglued areas are also put into the FEA model as measured.
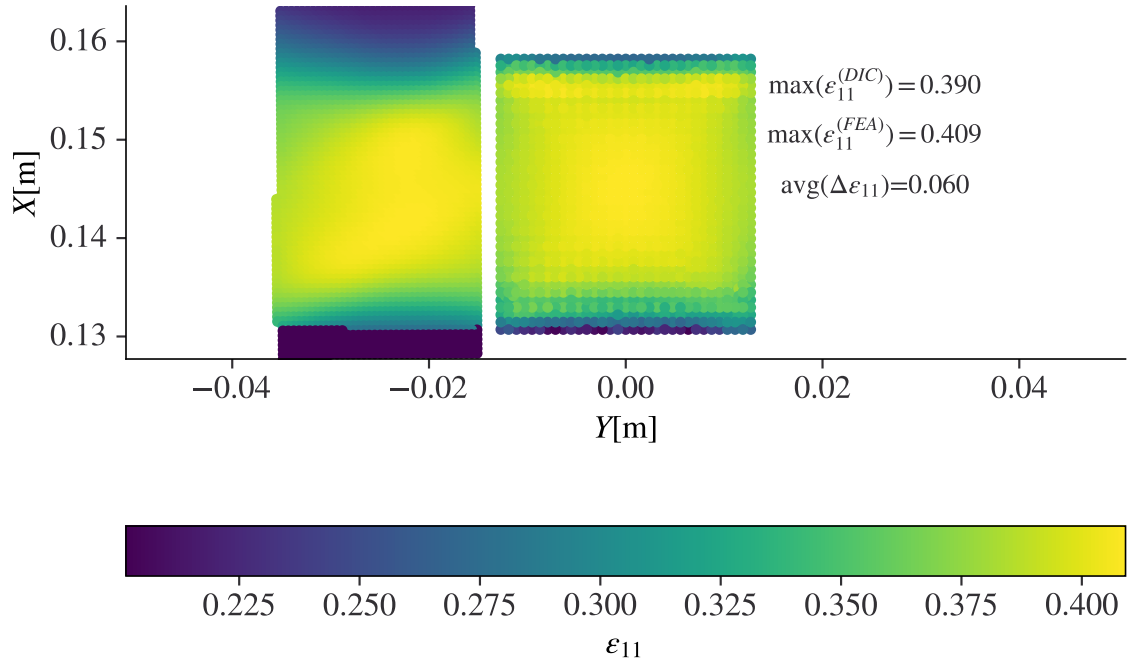
Figure 5.5: DIC and FEA undeformed data points with deformed data.

Once these nodes' values are calculated, the coarser FEA mesh has strains linearly interpolated to the finer DIC mesh (see Figure 5.5). Overall, the absolute average X-axis strain error (see Equation 5.1a) is a small value of 6% strain. The maximum X-axis strain for the FEA model is 40.9% strain and for the DIC is 39%, which is a strain error of 1.9%. This difference is strain is almost exclusively in the unglued region, which is likely from the lack of friction.

$$\text{mean}\left(\left|\Delta\epsilon_{11}(X_i^{(DIC)}, Y_i^{(DIC)})\right|\right) \tag{5.1a}$$

54

6. OPTIMIZATION RESULTS

6.1   Optimization

The optimization methodology chosen in Section 3.5.4 was followed. Two sets of optimization studies will be performed. Each set has random design vector ($\vec{D}$) guesses for the first generation. One will have the full range for each design variable, while the other will have a reduced range for SL thickness (t_{SL}). If both sets arrive at similar best solutions, which they did (see Section 6.4), then the best array of design variables of the two is more likely to remain the best with more sets/runs. However, if they did not converge to the same solution while both have low SL thicknesses, then an increase in population size or generations would be repeated until the two sets converge on a solution. If they did not converge while the first set has a high SL thickness, then the best design overall will be selected. During optimization, the rate of designs numerically converging instead of failing was tracked. Figure 6.1 shows the generated designs congregating into point clouds. These clouds will be talked about in Section 6.5.
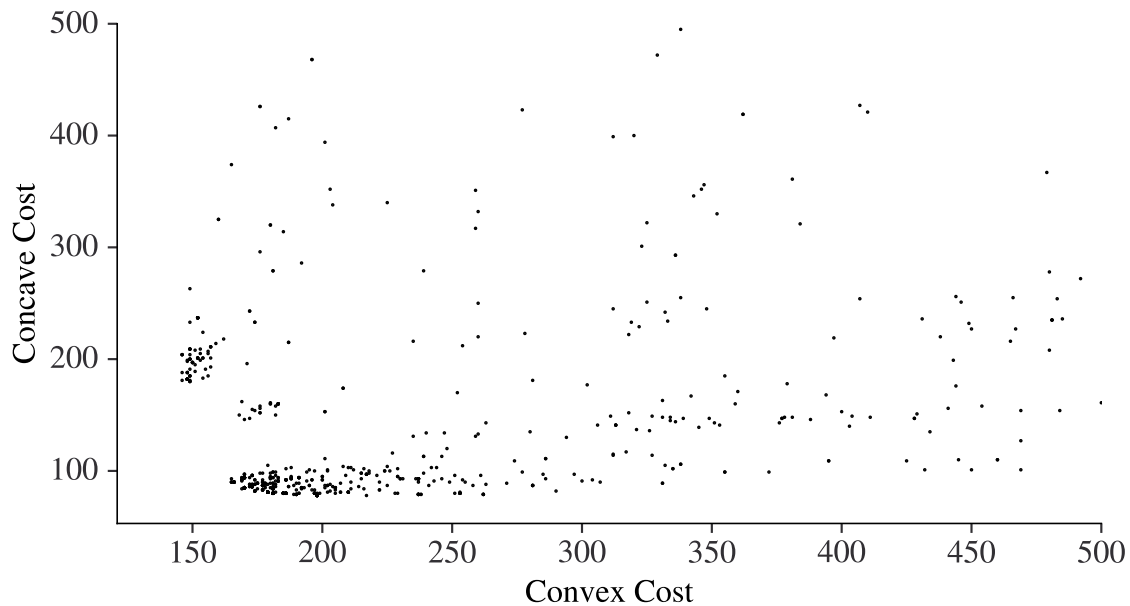
Figure 6.1: Set 1 cost scatter plot

55

6.1.1   Set 1

In the first set of optimization shown in Figure 6.2, 1000 runs converged to the solution shown in Table 6.1. In this first set, the optimization started numerically converging more often around the 250th run. This set had both the approximate best designs for both costs, seen in Section 6.3. The utopia point is created as described in Equation 3.6. The design closest to the utopia point is considered the approximate best design.
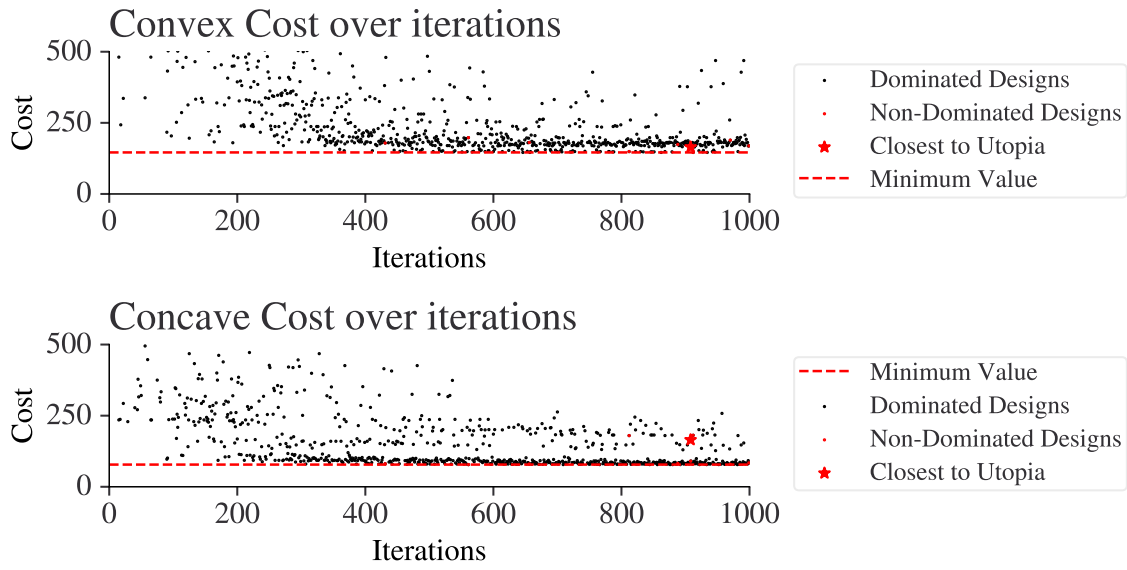
Figure 6.2: The convergence of the first optimization set

Table 6.1: Meaning of DV and the costs for Optimization Set 1

$\vec{D}$	$(3, 2, 2, 0, 4, 4, 2, 8)$
Means	$2O_i/\Delta X = (48, 42, 42)[\%]$
	$t_i = (0.25, 0.25, 0.25)[\text{in}]$
	$\epsilon^{(pre)} = 20\%$
	$t_{SL} = 0.12[\text{in}]$
$\vec{C}$	$(165, 90) \ [\text{m}^{-1}]$

6.1.2   Set 2

In the second set of optimization shown in Figure 6.3, 1440 runs converged to the solution shown in Table 6.2 using the utopia point of the first set. This second set of optimization was limited to an interpolating value of 5 for the Surface Layers thickness. There was no initialization seed given. These runs only numerically converged more often than not after the 400th run.
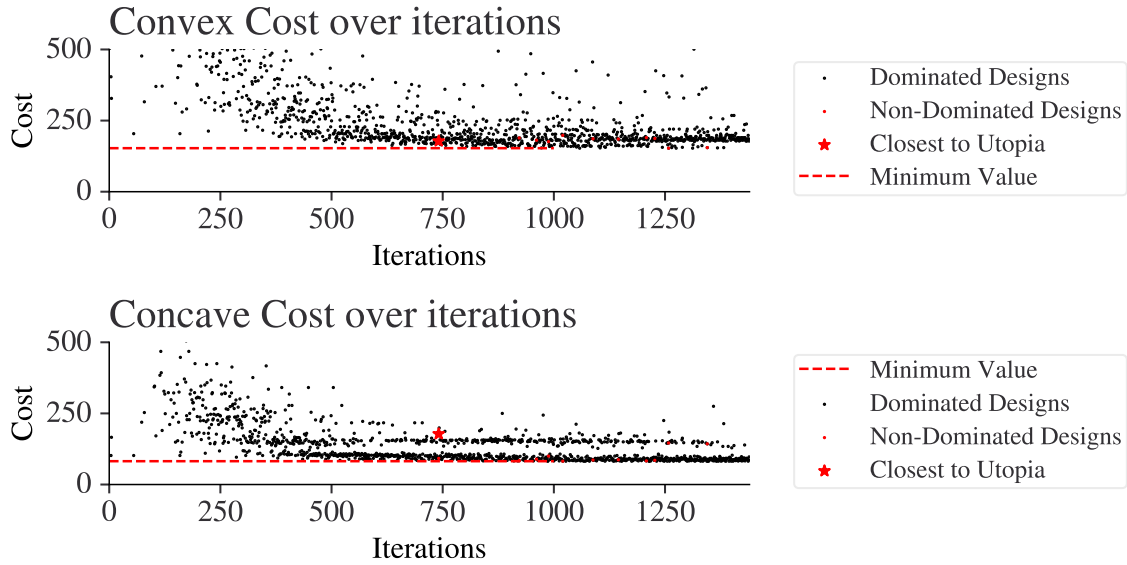
Figure 6.3: The convergence of the second optimization set

Table 6.2: Meaning of DV and the costs for Optimization Set 2

$\vec{D}$	$(3, 2, 2, 0, 4, 4, 2, 5)$
Means	$2O_i/\Delta X = (48, 42, 42)[\%]$
	$t_i = (0.25, 0.25, 0.25)[\text{in}]$
	$\epsilon^{(pre)} = 20\%$
	$t_{SL} = 0.097[\text{in}]$
$\vec{C}$	$(178, 92)\ [\text{m}^{-1}]$

57

6.2   Pareto Frontier

2440 designs were tested for optimization. The Pareto frontier in Figure 6.4 was constructed using the optimization results from Figures 6.2 and 6.3. The tails of the Pareto frontier are the approximate best designs for each configuration, expanded upon in Section 6.3. The utopia point is created by these tails and the closest design to it is also explained in that section. There are three distinct clouds of points that form near the Pareto frontier, though the one formed near the utopia point is much larger than the other two. This particular point cloud is studied in Section 6.5.
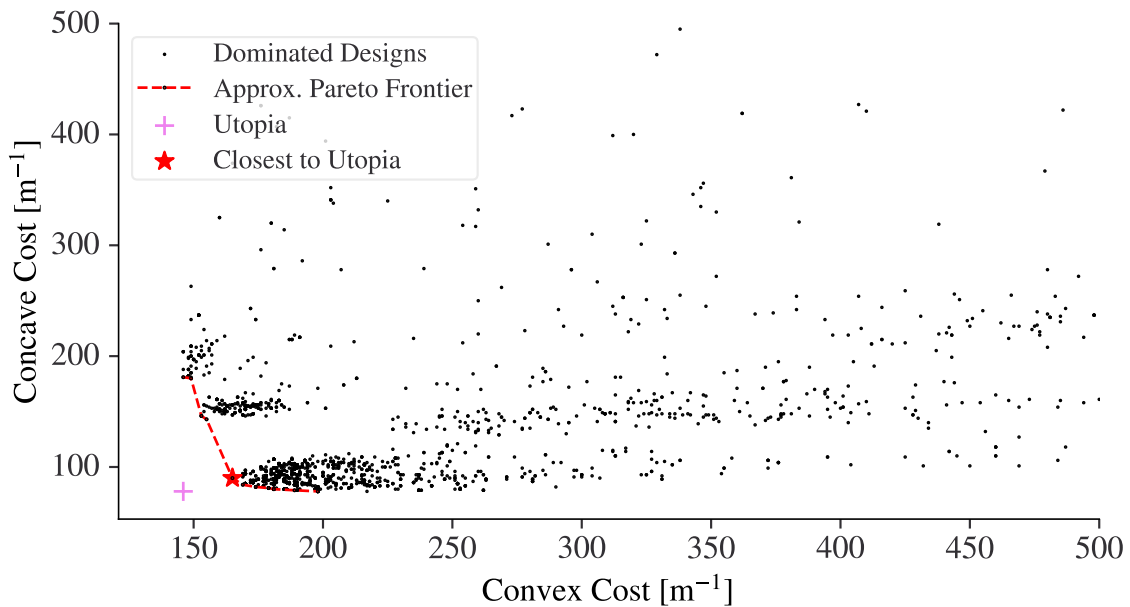
Figure 6.4: The Pareto frontier of both sets

6.3   Approximate Best Design for Each Configuration

6.3.1   Concave

This solution for the approximate best design for the concave configuration has a lot of overhang between panels two and three, as seen in Figure 6.5 and table 6.3. There is little overhang from panel one, though. The SRL is at its thinnest possible thickness and the Surface Layers is

rather thick, but not the the thickest that it could be. Pre-strain is low due to the large elongation between the overhangs of the first two panels.

Figure 6.5: The approximate best design for the concave configuration

6.3.2 Convex

The approximate best design for the convex configuration worked well because of the large amount of pre-strain, as seen in Figure 6.6 and Table 6.3. The large amount of inclination between the first two plates was countered with the pre-strain and small overhang. The second and third panel turned away from each other, meaning that the overhang between them could be larger. The thicknesses were found to be best when thin, but not the thinnest, and equal. The Surface Layers is at the same thickness value as the approximate best concave configuration.
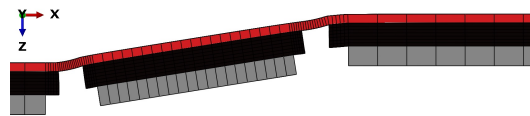
Figure 6.6: The approximate best design for the convex configuration

Table 6.3: Best Designs for the concave and convex

	Concave		Convex
$\vec{D}$	$(2, 5, 5, 0, 4, 4, 2, 7)$	$\vec{D}$	$(2, 1, 5, 1, 4, 4, 5, 7)$
Means	$2O_i/\Delta X = (42, 60, 60)[\%]$ $t_i = (0.25, 0.25, 0.25)[\text{in}]$ $\epsilon^{(pre)} = 20\%$ $t_{SL} = 0.11[\text{in}]$	Means	$2O_i/\Delta X = (42, 36, 60)[\%]$ $t_i = (0.3, 0.3, 0.3)[\text{in}]$ $\epsilon^{(pre)} = 50\%$ $t_{SL} = 0.11[\text{in}]$
$C_{concave}$	$(78)\ [\text{m}^{-1}]$	C_{convex}	$(146)[\text{m}^{-1}]$

6.4   Approximate Best Overall Design

The approximate best overall design from Table 6.1 in the concave configuration is in Figure 6.7. It is seen that the overhang of the SRL relaxes the transition between the Surface Layers above the panel and the Surface Layers between panels similar to 6.5. However, the size of the overhangs is smaller than in the approximate best concave design. In the convex configuration in Figure 6.8, the high pre-strain allows the out of plane deformation between plates turning into each other to be minimal. However, the bump between the first and second panels is more noticeable than in the approximate best convex configuration. Finally, the flat configuration Figure 6.9 reveals that all the Stress-Relieving Layers are the same height and have similar SRL overhang.
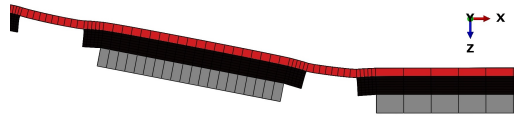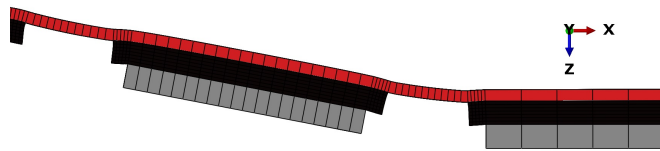

Figure 6.7: The approximate best design in the concave configuration
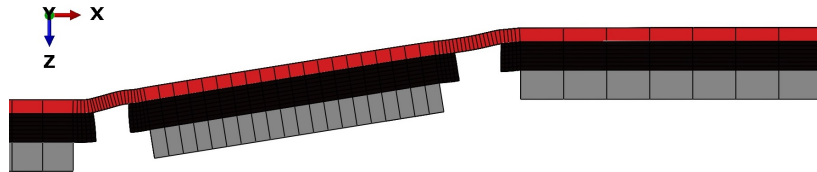
Figure 6.8: The approximate best design in the convex configuration

Figure 6.9: The approximate best design in the flat configuration, 3 panels

As seen in Tables 6.1 and 6.2, the best arrays of design variables found in each optimization set was only different in one variable: The thickness of the Surface Layers. This means that two separate optimizations found exactly the same SRL and pre-strain. This design is thus more likely to be the actual best design possible using the current FEA model and optimization method.

60

6.5   The Utopia Point

The distance between the utopia point and the approximate best design is approximately 22. This is a very short distance, about half the value of λ [m $^{-1}$], meaning that the approximate best overall design is not considerably worse than either of the approximate best designs for each configuration. Previously, in Section 4, costs could vary by the thousands. However, this design is not an anomaly. Around the utopia point is a cloud of low-cost designs, as seen in the zoomed in Figure 6.4. This cloud of low-cost designs contain various $\vec{D}$, not just the approximate best one or ones similar to it. This is seen in the closest six designs to the utopia point, shown in Table 6.4. Some designs are roughly equivalent (*) to the chosen best design in distance, but the full float value is slightly higher.

Table 6.4: Six nearest designs to the utopia point

$\vec{D}$	C_{convex} [m $^{-1}$]	$C_{concave}$ [m $^{-1}$]	Distance [m $^{-1}$]
$(2, 2, 5, 0, 4, 4, 2, 8)$	170	85	25
$(1, 2, 5, 0, 4, 4, 2, 8)$	173	86	28
$(2, 2, 1, 0, 4, 4, 2, 8)$	165	93	24
$(2, 2, 2, 0, 4, 4, 2, 8)$	166	90	23
$(2, 2, 2, 0, 4, 4, 2, 9)$	165*	90	22*
$(2, 2, 5, 0, 4, 4, 2, 8)$	170	85	25

These designs have one major thing in common: the SRL is always the same height. This means that the number of possible designs could have been significantly reduced in size (10^8 designs vs 10^6 designs) by removing (t_2, t_3) as design variables. If they were set to be equal to t_1, the designs would still result in low costs. However, there are designs in the cloud with different heights for each SRL segment.

6.6   Sources of Error

6.6.1   Material Properties

The material properties of the hyper-elastic SL and the rubber-foam SRL were not measured at multiple strain rates nor at high sample rates. This means that Abaqus has to use the one set of sparse data to estimate material response values during the runs. Also, the MTS testing of the silicone rubber did not go past $+200\%$ strain, losing valuable insight for the Abaqus model. This error could be accounted for with more thorough material testing.

6.6.2   Reduced vs Full Integration

Three random low cost designs from the optimization in Section 6 were tested with C3D8 and C3D8R elements in the convex and concave configurations to see the cost differences, ΔC [m $^{-1}$] . It took a total of 14 minutes to run the designs with C3D8R elements and 24 minutes to run the designs with C3D8 elements, with each configuration taking 4 minutes in C3D8 and approximately 2 minutes in C3D8R. While the reduced integration elements were far quicker to run, the loss in accuracy is clearly visible in all of the runs. This is shown in Table 6.10. While all designs decreased in cost, some decreased notably more than others. It is likely that using this method would have the precise optimization method find a new approximate best design.
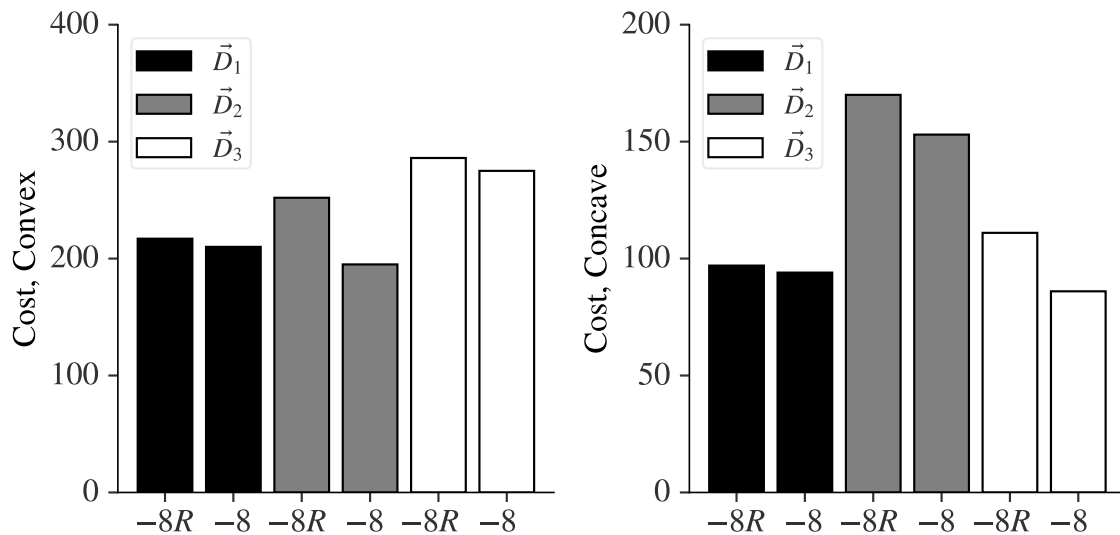
Figure 6.10: The costs going from C3D8R (-8R) to C3D8 (-8) for three designs

6.6.3   Levels

The levels of the DVs allowed for simplified coding, more diverse exploration, and easy DOE comparisons for such large ranges. However, they prevent designs that fall between the levels. This limits the optimization method from finding better designs between the levels. Another study with these limitations removed would likely find a solution similar, and superior to, the cloud of designs in Section 6.5 and the approximate best design.

6.6.4   Construction

The first prototype, as seen on the left in Figure 1.3, revealed many sources of possible error. One that was addressed in this thesis is the detachment of the layers due to failed adhesion. These issues with the adhesive were mitigated with the adhesive testing in Section 4.1.3. However, another source of observed error in the FEA model that was not modelled are the hinges. The first prototype would bend the hinges when it moved into the convex configuration, as shown in Figure 3.3. It is likely that the current hinges will bend again if the new approximate best design was applied. The hinges are liable to change. Modelling of the hinges in concert with the kinematic model from the panel team could assist in redesigning these hinges to handle the conformal layer.

The construction of the prototype used for DIC testing was not perfect. The unglued area was significant in the error value, as was seen in Section 5.1.1. It was found that the error with the normal model was significant, which is concerning, but it was mitigated by modelling the unglued area itself. In order to have perfect validation, however, the sample must have no issues. Thus, future work will include a properly constructed and tested prototype.

7. CONCLUSIONS AND FURTHER STUDY

7.1 Conclusion

An approximate best design for the conformal layer of a supersonic morphing aircraft has been designed in FEA and validated with a simplified testing prototype. This design creates the smooth OMLs seen in Figure 7.1. The conformal layer was split into two layers, the hyper-elastic Surface Layer and the foam-rubber Stress-Relieving Layer. The Surface Layer material was a hyper-elastic Silicone Rubber that handled the large strains. The Stress Relieving Layer was an EDPM foam rubber that supported the Surface layer both on and off of the panel. This conformal layer was loaded with the maximum expected pressure load of 0.5[psi], attached to a five panel system, and was strained up to 200%. The Surface Layer and Stress-Relieving Layer were sized and shaped through an optimization methodology utilizing NSGA-II. This methodology created a front of designs that were non-dominated. Of these, the conformal layer matched the contour of a design. That design is equally good at minimizing the cost function in two different panel configurations. The Stress-Relieving Layer design and the pre-strain of the Surface Layer were the same in two different optimization sets, demonstrating the precision of the current model. Sources of error were identified and mitigation strategies were put into place, but a few sources of error remain.

(a) Convex (b) Concave
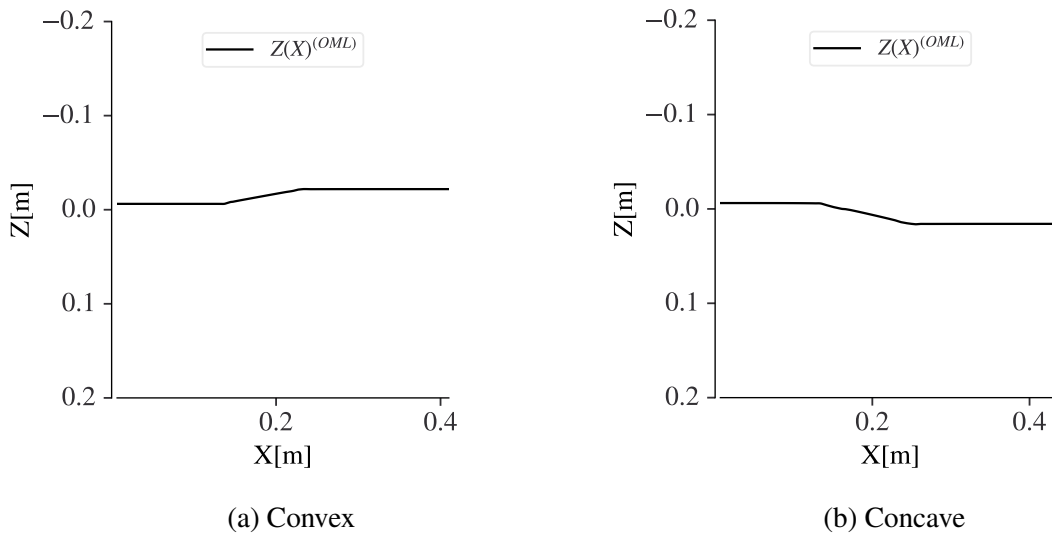
Figure 7.1: Best designs Z(X) for the Outer Mold Line (OML).

7.2 Further Study

There are three components to further the current model. First, the removal of the levels would allow for the exploration of designs similar the current best approximate design and to those in Table 6.4. It is very likely that there is a design that costs less than the current design hidden between the levels, just as this design costs slightly less than a design in 6.5. Second, the use of C3D8 elements to increase the accuracy of the model. Third, a more thorough exploration of the material properties of selected materials for a more accurate model of the real system.

This current model works well without topology optimization, but topology optimization using SPIDRS and/or Tosca could be applied to reinforce the weaknesses of the best design. For SPIDRS, small connections may help significantly between the panels as in Figure 3.25. For Tosca, the distribution of matter could greatly refine a fully constructed model.

The current model does not consider dynamic flow. Having computational fluid dynamics (CFD) run either simultaneously or in step with the model would be of great use in the reduction of noise on the ground. For example, the cost function could be improved upon by taking into account the actual perceived loudness in decibel measured on the ground for every design. Additionally, transverse shear loading and dynamic pressure loading from fluid dynamic analysis can be applied to the Surface Layer to better determine the amount of reinforcement required for this material. The reinforcement could take on the form of spherical inclusions, fibers, or even turning the Surface Layer into a composite.

REFERENCES

[1] *Code of Federal Regulations*, vol. 2. Government Publishing Office, 1-1-22 ed., 2022.

[2] P. B. C. Leal, J. A. Schrass, T. N. Giblette, D. F. Hunsaker, H. Shen, T. S. Logan, and D. J. Hartl, "Effects of atmospheric profiles on sonic boom perceived level from supersonic vehicles," *AIAA Journal*, vol. 59, no. 12, pp. 5020–5028, 2021.

[3] J. M. Weaver-Rosen, F. L. Carpenter, P. G. Cizmas, R. J. Malak, T. A. Abraham, D. F. Hunsaker, and D. S. Lazzara, "Computational design methodology of adaptive outer mold line for robust low en-route noise of a supersonic aircraft," in *AIAA Scitech 2021 Forum*, AIAA, 2021.

[4] J. A. Schrass, P. B. Leal, and D. J. Hartl, "Structurally feasible morphing of a low-boom supersonic transport," in *AIAA Scitech 2020 Forum*, AIAA, 2020.

[5] B. D. Kocher, P. A. Kreth, J. D. Schmisseur, E. J. LaLonde, and C. S. Combs, "Characterizing streamwise development of surface roughness effects on a supersonic boundary layer," *AIAA Journal*, vol. 60, no. 9, pp. 5136–5149, 2022.

[6] J. D. Anderson, *Fundamentals of Aerodynamics*. McGraw Hill Education, 6 ed., 2017.

[7] B. Zhao, M. Qi, H. Sun, X. Shi, and C. Ma, "A comprehensive analysis on the structure of groove-induced shock waves in a linear turbine," *Aerospace Science and Technology*, vol. 87, pp. 331–339, 2019.

[8] T. Egbert, *Essentials of Supersonic Commercial Aircraft Conceptual Design*. Aerospace Series, Wiley, first ed., 2020.

[9] J. W. Pawlowski, "Origins and overview of the shaped sonic boom demonstration program," in *NASA Technical Reports*, NASA, 2005. Access URL: https://ntrs.nasa.gov/citations/20050165091.

[10] D. A. Burdette and J. R. Martins, "Design of a transonic wing with an adaptive morphing trailing edge via aerostructural optimization," *Aerospace Science and Technology*, vol. 81, pp. 192–203, 2018.

[11] C. R. Bolander, D. F. Hunsaker, H. Shen, and F. L. Carpenter, "Procedure for the calculation of the perceived loudness of sonic booms," in *AIAA Scitech 2019 Forum*, AIAA, 2019.

[12] T. Abraham, "Sonic boom loudness reduction through localized supersonic aircraft equivalent-area changes," *All Graduate Theses and Dissertations*, 2021.

[13] T. N. Giblette, "Rapid prediction of low-boom and aerodynamic performance of supersonic transport aircraft using panel methods," *All Graduate Theses and Dissertations*, 2019.

[14] W. Li and S. Rallabhandi, "Inverse design of low-boom supersonic concepts using reversed equivalent-area targets," *Journal of Aircraft*, vol. 51, no. 1, pp. 29–36, 2014.

[15] S. L. Garrett, *Understanding Acoustics:An Experimentalist's View of Sound and Vibration*. Springer Nature, 2 ed., 2020.

[16] W. A. Willis, J. M. Cormack, C. E. Tinney, and M. F. Hamilton, "Reduced-order comparison of simulated and measured coalescing mach waves near supersonic jets," *AIAA Journal*, vol. 61, no. 5, pp. 2022–2034, 2023.

[17] D. e. Lagoudas, *Shape Memory Alloys: Modeling and Engineering Applications*. Springer New York, NY, first edition ed., 2008.

[18] C. L. Bertagne, D. J. Hartl, and T. J. Cognata, "Analysis of highly coupled thermal-structural responses in morphing radiative bodies," in *23rd AIAA/AHS Adaptive Structures Conference*, AIAA, 2015.

[19] M. Baniasadi, Z. Xu, S. Hong, M. Naraghi, and M. Minary-Jolandan, "Thermo-electromechanical behavior of piezoelectric nanofibers," *ACS Applied Materials & Interfaces*, vol. 8, no. 4, pp. 2540–2551, 2016. PMID: 26795238.

[20] J. Vůjtěch, P. Ryjáček, J. Campos Matos, and E. Ghafoori, "Iron-based shape memory alloy for strengthening of 113-year bridge," *Engineering Structures*, vol. 248, p. 113231, 2021.

[21] G. Eggeler, E. Hornbogen, A. Yawny, A. Heckmann, and M. Wagner, "Structural and functional fatigue of niti shape memory alloys," *Materials Science and Engineering: A*, vol. 378, no. 1, pp. 24–33, 2004. European Symposium on Martensitic Transformation and Shape-Memory.

[22] W. Zuk, *Kinetic Architecture*. Van Nostrand Reinhold, 1970.

[23] F. Geiger, J. Gade, M. von Scheven, and M. Bischoff, "Optimal design of adaptive structures vs. optimal adaption of structural design," *IFAC-PapersOnLine*, vol. 53, no. 2, pp. 8363–8369, 2020. 21st IFAC World Congress.

[24] P. Zhang, J. Li, and M. Chen, "Effect of different temperatures on the metallographic structure and tensile property of 2024-t4 alloy in integral heating single point incremental forming.," *Microscopy Research and Technique*, vol. 83, no. 8, p. 920, 2020.

[25] H. Basaeri, A. Yousefi-Koma, M. R. Zakerzadeh, and S. S. Mohtasebi, "Experimental study of a bio-inspired robotic morphing wing mechanism actuated by shape memory alloy wires," *Mechatronics*, vol. 24, no. 8, pp. 1231–1241, 2014.

[26] P. A. L. S. Martins, R. M. Natal Jorge, and A. J. M. Ferreira, "A comparative study of several material models for prediction of hyperelastic properties: Application to silicone-rubber and soft tissues," *Strain*, vol. 42, no. 3, pp. 135–147, 2006.

[27] B. Erman and J. E. Mark, *Structures and Properties of Rubberlike Networks*. Oxford University Press, 08 1997.

[28] R. Wu, J. Sun, Z. Chang, R. Bai, and J. Leng, "Elastic composite skin for a pure shear morphing wing structures," *Journal of Intelligent Material Systems and Structures*, vol. 26, no. 3, pp. 352–363, 2015.

[29] M. Z. Zakaria, H. Jamaluddin, R. Ahmad, and S. M. Loghmanian, "Comparison between multi-objective and single-objective optimization for the modeling of dynamic systems," *Pro-*

ceedings of the Institution of Mechanical Engineers, Part I: Journal of Systems and Control Engineering, vol. 226, no. 7, pp. 994–1005, 2012.

[30] R. Gorgin and W. Ziping, "Structural damage identification based on principal curvatures of mode shape.," *International Journal of Acoustics & Vibration*, vol. 25, no. 4, pp. 566 – 576, 2020.

[31] B. Szabó and I. Babuska, *Finite Element Analysis : Method, Verification and Validation*, vol. second edition of *Wiley Series in Computational Mechanics Series*. John Wiley & Sons, Incorporated, 2021.

[32] I. Magomedov and Z. Sebaeva, "Comparative study of finite element analysis software packages," *Journal of Physics: Conference Series*, vol. 1515, p. 032073, 04 2020.

[33] *Abaqus Documentation*. Dassault Systemes, 2021.

[34] Mengyinan, "Capability analysis of abaqus shell element based on finite element method," *Journal of Physics: Conference Series*, vol. 1345, p. 022034, 11 2019.

[35] T. C. Chu, W. F. Ranson, and M. A. Sutton, "Applications of digital-image-correlation techniques to experimental mechanics," *Experimental Mechanics*, vol. 25, pp. 232 – 244, 1985.

[36] M. Torres Arellano, L. Crouzeix, B. Douchin, F. Collombet, H. Hernández Moreno, and J. González Velázquez, "Strain field measurement of filament-wound composites at ±55° using digital image correlation: An approach for unit cells employing flat specimens," *Composite Structures*, vol. 92, no. 10, pp. 2457–2464, 2010.

[37] McMaster-Carr Supply Company, "McMaster-Carr website."

[38] Z. Zakaria, Z. Ariff, T. Hwa, and C. Sipaut, "Effect of foaming temperature on morphology and compressive properties of ethylene propylene diena monomer rubber (epdm) foam," *Malaysian Polymer Journal (MPJ)*, vol. 2, pp. 22–30, 01 2007.

[39] ASTM D, "Standard test method for apparent shear strength of single-lap-joint adhesively bonded metal specimens by tension loading (metal-to-metal)," *ASTM International*, 2019.

[40] G. Cho, Y. Kim, J. Kwon, W. Su, and M. Wang, "Impact of data sampling methods on the performance of data-driven parameter identification for lithium ion batteries," *IFAC-PapersOnLine*, vol. 54, no. 20, pp. 534–539, 2021. Modeling, Estimation and Control Conference MECC 2021.

[41] K. Deb, A. Pratap, S. Agarwal, and T. Meyarivan, "A fast and elitist multiobjective genetic algorithm: Nsga-ii," *IEEE Transactions on Evolutionary Computation*, vol. 6, no. 2, pp. 182–197, 2002.

[42] J. Blank and K. Deb, "pymoo: Multi-objective optimization in python," *IEEE Access*, vol. 8, pp. 89497–89509, 2020.

[43] M. Bendsøe and O. Sigmund, *Topology Optimization - Theory, Methods, and Applications*. Germany: Springer Verlag, 2003.

[44] B. R. Bielefeldt, E. Akleman, G. W. Reich, P. S. Beran, and D. J. Hartl, "L-System-Generated Mechanism Topology Optimization Using Graph-Based Interpretation," *Journal of Mechanisms and Robotics*, vol. 11, 02 2019. 020905.

[45] B. Bielefeldt, G. Reich, P. Beran, and D. Hartl, "Development and validation of a genetic l-system programming framework for topology optimization of multifunctional structures," *Computers & Structures*, vol. 218, 04 2019.

[46] M. Pagac, D. Schwarz, J. Petru, and S. Polzer, "3d printed polyurethane exhibits isotropic elastic behavior despite its anisotropic surface," *Rapid Prototyping Journal*, vol. ahead-of-print, 06 2020.

[47] M. Cheng and W. Chen, "Experimental investigation of the stress–stretch behavior of epdm rubber with loading rate effects," *International Journal of Solids and Structures*, vol. 40, no. 18, pp. 4749–4768, 2003.